

Mitigating numerical dissipation in simulations of subsonic turbulent flows

James Watt¹   Christoph Federrath¹   Claudio Birke² and Christian Klingenberg²

¹Research School of Astronomy and Astrophysics, Australian National University, Cotter Road, Canberra, ACT 2611, Australia

²Department of Mathematics, University of Würzburg, Sanderring 2, 97070 Würzburg, Germany

Accepted 2025 November 6. Received 2025 October 21; in original form 2025 March 19

ABSTRACT

Magnetohydrodynamic (MHD) simulations of subsonic (Mach number < 1) turbulence are crucial to our understanding of several processes including oceanic and atmospheric flows, the amplification of magnetic fields in the early universe, accretion discs and stratified flows in stars. In this work, we demonstrate that conventional numerical schemes are excessively dissipative in this low-Mach regime. We demonstrate that a new numerical scheme (termed ‘USM-BK’ and implemented in the FLASH MHD code) reduces the dissipation of kinetic and magnetic energy, constrains the divergence of magnetic field to zero close to machine precision, and resolves smaller-scale structure than other, more conventional schemes, and hence, is the most accurate for simulations of low-Mach turbulent flows among the schemes compared in this work. We first compare several numerical schemes/solvers, including Split-Roe, Split-Bouchut, USM-Roe, USM-HLLC, USM-HLLD, and the new USM-BK, on a simple vortex problem. We then compare the schemes/solvers in simulations of the turbulent dynamo and show that the choice of scheme affects the growth rate, saturation level, and viscous and resistive dissipation scale of the dynamo. We also measure the numerical kinematic Reynolds number (Re) and magnetic Reynolds number (Rm) of our otherwise ideal MHD flows, and show that the new USM-BK scheme provides the highest Re and comparable Rm among all the schemes compared.

Key words: magnetic fields – MHD – turbulence – methods: numerical.

1 INTRODUCTION

Subsonic flows are ubiquitous in a wide range of physical systems, ranging from terrestrial applications to astrophysics. They appear in the study of turbine blade performance (J. Leggett, Y. Zhao & R. D. Sandberg 2022), fusion and fission systems (M. Min et al. 2024), rotorcraft fuselages and ship airwakes (H. Park, D. Linton & B. Thorner 2022), ocean modelling (G. Tissot, É. Mémin & Q. Jamet 2024), stratified systems like stars (F. Kupka & H. J. Muthsam 2017), and the amplification of primordial magnetic fields (J. M. Wagstaff et al. 2014; R. Achikanath Chirakkara et al. 2021). Such subsonic flows are characterized by fluid velocities smaller than the speed of sound (also referred to as the low-Mach regime, where Mach number $M = v/c_s < 1$ and v and c_s are flow velocity and sound speed, respectively). Being inherently non-linear and three-dimensional, these turbulent, complex systems are impossible to tackle via analytic calculations. Hence, they are studied through numerical simulations, a large class of which use finite-volume discretization and Godunov-based methods. While such methods are highly successful in modelling the transonic and the supersonic regime, they are subject to limitations in terms of efficiency in the subsonic regime. The artificial discontinuity created by the finite-volume method (FV method) at each cell interface creates spurious waves that lead to an overestimate of pressure, overwhelming the

physical fluxes (see H. Guillard & A. Murrone 2004), leading to excessive dissipation in the low-Mach regime. Apart from this, the discretization of the magnetohydrodynamic (MHD) equations introduces viscous terms as well (see L. Malvadi Shivakumar & C. Federrath 2023). Both of these effects combined operate similar to physical viscosity (ν) and resistivity (η), and are referred to as artificial and numerical viscosity and resistivity.

These types of numerical/artificial viscosity and resistivity must be significantly lower than the physical viscosity and resistivity simulations aiming to resolve down to the physical dissipation scale. Otherwise, small-scale features of the flow are smeared out. Flow properties in MHD are determined primarily by the hydrodynamic and the magnetic Reynolds numbers, labelled Re and Rm, respectively. They are defined as

$$\text{Re} = \frac{u\ell}{\nu}, \text{ and} \quad (1)$$

$$\text{Rm} = \frac{u\ell}{\eta}, \quad (2)$$

where u and ℓ are the characteristic velocity and length scales of the flow, respectively. To accurately model a flow, the numerical Re and Rm must be larger than the physical Re and Rm of the flows being modelled.

Numerical dissipation arising from discretization can be reduced by increasing the grid resolution and special techniques, like Adaptive Mesh Refinement (M. J. Berger & P. Colella 1989). The effect of grid resolution on numerical viscosity and resistivity has been thoroughly studied by L. Malvadi Shivakumar & C. Federrath (2023).

* E-mail: James.Watt@anu.edu.au (JW); christoph.federrath@anu.edu.au (CF)

In this work, we focus on the dissipation originating from the artificial discontinuities created by the FV method in simulating subsonic flows. We test an extension of K. Waagan, C. Federrath & C. Klingenberg (2011) introduced in C. Birke & C. Klingenberg (2023), which significantly reduces this dissipation.

In Section 2, we introduce the MHD equations. Section 3 describes our numerical methods and briefly summarizes why simulations of subsonic flows are more dissipative and how C. Birke & C. Klingenberg (2023) overcome this difficulty. Section 4 presents simulations of the Balsara vortex (D. S. Balsara 2004, see also G. Leidi et al. 2022) as a test case for a variety of numerical schemes, all at the same grid resolution, to demonstrate the effect of the choice of numerical scheme on artificial viscosity and resistivity and test if the new scheme provides an improvement over previous methods. In Section 5, we test the various numerical schemes on simulations of subsonic turbulent dynamos, which also have important astrophysical applications. We compare the effect of the numerical scheme on the time evolution and saturation of the dynamo, as well as the structure and turbulent MHD statistics of the system. We also measure the numerical Reynolds numbers of these otherwise ideal MHD ($\text{Re} \rightarrow \infty$, $\text{Rm} \rightarrow \infty$) simulations. We summarize our results in Section 6.

2 EQUATIONS OF MHD

The MHD equations are given as follows:

$$\frac{\partial \rho}{\partial t} + \nabla \cdot (\rho \mathbf{u}) = 0, \quad (3)$$

$$\begin{aligned} \frac{\partial}{\partial t} (\rho \mathbf{u}) + \nabla \cdot \left(\rho \mathbf{u} \otimes \mathbf{u} - \frac{1}{4\pi} \mathbf{B} \otimes \mathbf{B} \right) + \nabla p_{\text{tot}} \\ = \nabla \cdot (2\nu \rho \mathbf{S}) + \rho \mathbf{F}, \end{aligned} \quad (4)$$

$$\frac{\partial e}{\partial t} + \nabla \cdot \left[(e + p_{\text{tot}}) \mathbf{u} - \frac{1}{4\pi} (\mathbf{B} \cdot \mathbf{u}) \mathbf{B} \right] = \quad (5)$$

$$\begin{aligned} \nabla \cdot \left[2\nu \rho \mathbf{u} \cdot \mathbf{S} + \frac{1}{4\pi} \eta \mathbf{B} \times (\nabla \times \mathbf{B}) \right], \\ \frac{\partial}{\partial t} \mathbf{B} = \nabla \times (\mathbf{u} \times \mathbf{B}) + \eta \nabla^2 \mathbf{B}. \end{aligned} \quad (6)$$

Here, ρ , \mathbf{u} , $p_{\text{tot}} = p_{\text{th}} + |\mathbf{B}|^2/(8\pi)$, \mathbf{B} , $e = \rho e_{\text{int}} + \rho |\mathbf{u}|^2/2 + |\mathbf{B}|^2/(8\pi)$, $\mathbf{S}_{ij} = (\partial_i u_j + \partial_j u_i)/2 - (\delta_{ij} \nabla \cdot \mathbf{u})/3$, ν , η denote the density, velocity, pressure (thermal plus magnetic), magnetic field, energy density (internal plus kinetic, plus magnetic), strain tensor, kinematic viscosity, and magnetic resistivity, respectively. The system of equations is closed by an equation of state relating the thermal pressure (p_{th}) to the density (ρ).

The magnetic field also satisfies the divergence free constraint given by

$$\nabla \cdot \mathbf{B} = 0. \quad (7)$$

In the absence of physical viscosity and resistivity ($\nu = 0$ and $\eta = 0$), the system of partial differential equations described above takes the general conservative form

$$\frac{\partial \mathbf{U}}{\partial t} + \frac{\partial \mathbf{F}}{\partial x} + \frac{\partial \mathbf{G}}{\partial y} + \frac{\partial \mathbf{H}}{\partial z} = 0, \quad (8)$$

where \mathbf{U} is a vector of conservative variables given by

$$\mathbf{U} = [\rho, \rho u_x, \rho u_y, \rho u_z, e, B_x, B_y, B_z], \quad (9)$$

and \mathbf{F} , \mathbf{G} , and \mathbf{H} are the fluxes given by

$$\begin{aligned} \mathbf{F} = [\rho v_x, \rho v_x^2 + p_{\text{th}} + |\mathbf{B}|^2/8\pi - B_x^2/4\pi, \rho v_x v_y - B_x B_y/4\pi, \\ \rho v_x v_z - B_x B_z/4\pi, (e + p_{\text{th}} + |\mathbf{B}|^2/8\pi) v_x - B_x (\mathbf{v} \cdot \mathbf{B})/4\pi, 0, \\ (v_x B_y - v_y B_x), -(v_z B_x - v_x B_z)], \end{aligned} \quad (10)$$

$$\begin{aligned} \mathbf{G} = [\rho v_y, \rho v_x v_y - B_x B_y/4\pi, \rho v_y^2 + p_{\text{th}} + |\mathbf{B}|^2/8\pi - B_y^2/4\pi, \\ \rho v_y v_z - B_y B_z/4\pi, (e + p_{\text{th}} + |\mathbf{B}|^2/8\pi) v_y - B_y (\mathbf{v} \cdot \mathbf{B})/4\pi, 0, \\ (v_y B_z - v_z B_y), -(v_x B_y - v_y B_x)], \end{aligned} \quad (11)$$

$$\begin{aligned} \mathbf{H} = [\rho v_z, \rho v_x v_z - B_x B_z/4\pi, \rho v_y v_z - B_y B_z/4\pi, \\ \rho v_z^2 + p_{\text{th}} + |\mathbf{B}|^2/8\pi - B_z^2/4\pi, (e + p_{\text{th}} + |\mathbf{B}|^2/8\pi) v_z - B_z (\mathbf{v} \cdot \mathbf{B})/4\pi, 0, \\ (v_x B_z - v_z B_x), -(v_y B_z - v_z B_y)]. \end{aligned} \quad (12)$$

3 NUMERICAL METHODS

3.1 Finite volume method

Equation (8) can be solved using the finite-volume (FV) method. The FV method divides the computational domain into control volumes (grid cells) and integrates the governing equations over each volume, ensuring conservation of fluxes across cell boundaries. Fluxes at the interfaces are computed using Riemann solvers (such as Roe, HLLD, HLLC, etc). To improve accuracy, the physical state variables are reconstructed at the cell faces via linear or even higher-order reconstruction. Slope limiters are used to ensure that the reconstruction step does not introduce artificial maxima/minima. The temporal discretization is performed using schemes such as Euler or Runge–Kutta methods and the time-stepping can be implemented in a split or unsplit fashion. The divergence of the magnetic field is constrained to zero up to machine precision using constrained transport (CT) (K. Yee 1966; C. R. Evans & J. F. Hawley 1988; W. Dai & P. R. Woodward 1998; T. A. Gardiner & J. M. Stone 2008), or kept at reasonably low levels by a divergence cleaning technique (A. Dedner et al. 2002).

3.2 Numerical dissipation

Discretization of MHD equations gives rise to viscous terms that introduce numerical dissipation. This kind of numerical dissipation can be reduced by choosing a reconstruction method or a time stepper of higher order. However, finite-volume methods also create an artificial discontinuity at each grid interface that gives rise to spurious waves. Since these artificial waves create pressure fluctuations of the order of the sonic Mach number M , they can overwhelm the physical flux in the simulations of low-Mach flows that have pressure fluctuations of the order M^2 (H. Guillard & A. Murrone 2004). This leads to excessive dissipation in low-Mach flows. Various methods have been explored to mitigate this issue, like pre-conditioning the Riemann problem at each interface to reduce the effect of discontinuities (E. Turkel 1999; S. Clerc 2000), or rescaling the dissipation term in the numerical flux to make it independent of the Mach number (F. Miczek, F. K. Röpke & P. V. F. Edelmann 2015; T. Minoshima & T. Miyoshi 2021; G. Leidi et al. 2022; C. Birke, C. Chalons & C. Klingenberg 2023). Another approach is the use of implicit–explicit methods, which apply the Godunov-type scheme only to the slow dynamics in the PDE, thereby avoiding dissipation

terms that scale with $O(1/M)$ (R. Klein 1995; M. Dumbser et al. 2018; F. Fambri 2021; W. Chen, K. Wu & T. Xiong 2023; C. Birke, W. Boscheri & C. Klingenberg 2024; W. Boscheri & A. Thomann 2024). Building on this idea, F. Fambri & E. Sonnendrücker (2024) employ implicit-explicit methods in combination with the Finite Element method for solving the magneto-acoustic parts, ensuring energy stability, magnetic-helicity conservation, and a divergence-free magnetic field. Alternatively, J.-M. Teissier, R. Mäusle & W. C. Müller (2024) reduce artificial and numerical viscosity through very high-order reconstruction methods, and improve efficiency by reconstructing separately in each spatial dimension rather than using multidimensional polynomials. In this work, we focus on the relaxation scheme by C. Birke & C. Klingenberg (2023) (referred to as the BK method), which resorts on rescaling the numerical flux in the low-Mach-number regime.

3.3 BK method

The core idea of the BK method is to construct an enlarged system of equations, including a relaxation term on the right-hand side, such that the new system is an approximation of the original system given in Section 2. Then the left-hand side of the relaxation system is solved using a Riemann solver followed by a projection of the solution back on to the original variables. Since there is some freedom in how the relaxation system is constructed, it is possible to tweak the solution of the pressure variable in the Riemann fan and fix the incorrect scaling of the pressure, while ensuring that the resulting Riemann solver satisfies a discrete entropy inequality. We point the reader to C. Birke & C. Klingenberg (2023) for further details on their relaxation scheme.

The fastest wave-speed in the Riemann fan of the BK relaxation scheme can be closely approximated by

$$\lambda_{\text{fastest}} = u + \frac{1}{2} \sqrt{\left(\frac{c_s^2}{M_{\text{BK}}^2} + c_A^2 \right)} + \sqrt{\left(\frac{c_s^2}{M_{\text{BK}}^2} + c_A^2 \right)^2 - 4c_s^2 c_{A;x}^2}, \quad (13)$$

where u is the fluid velocity, c_s is the sound speed, c_A is the Alfvén speed, $c_{A;x}$ is the Alfvén speed in the x -direction (direction along which the MHD equations are one-dimensionalized before solving the Riemann problem) and M_{BK} (the equivalent of ϕ in equations (14)–(16) in C. Birke & C. Klingenberg 2023) is defined as

$$M_{\text{BK}} = \min \left\{ \max \left\{ M_{\text{cut}}, \frac{u}{c_s} \right\}, 1 \right\}. \quad (14)$$

The parameter $M_{\text{cut}} < 1$ is used to set a local cut-off Mach number below which the scheme does not reduce dissipation any longer by increasing the scheme-specific speed, thereby preventing division by small numbers in regions where the velocity is close to 0, which would lead to $\lambda_{\text{fastest}} \rightarrow \infty$ and the time-step $\Delta t \rightarrow 0$. In this work, we set M_{cut} equal to 2 times the reference Mach number ($\mathcal{M} = 0.1$ or 0.01) that we are simulating – the reference Mach number is a statistical (global) quantity describing the characteristic ratio of typical flow velocities to the sound speed in a given problem.¹ The reason for our choice of $M_{\text{cut}} = 2\mathcal{M}$ is explained in Appendix A. Note that for a conventional Riemann solver, like Roe or HLLD,

¹For instance, in turbulent flows, \mathcal{M} is the standard deviation of the local Mach number (M).

$M_{\text{BK}} = 1$, and λ_{fastest} is a close approximation of the fastest wave speed in the Riemann fan of these conventional solvers.

The time-step restriction for stability is given by the Courant-Friedrichs-Lowy (CFL) condition,

$$\Delta t = \text{CFL} \frac{\Delta x}{\lambda_{\text{fastest}}}, \quad (15)$$

where Δx is the cell size. We use $\text{CFL} = 0.5$ throughout this work.

3.4 Numerical schemes in FLASH

We perform our simulations using a modified version of the FLASH code (B. Fryxell et al. 2000; A. Dubey et al. 2008) and compare several numerical schemes with different Riemann solvers. Some schemes utilize split time-stepping combined with Dedner-Marder cleaning (B. Marder 1987; A. Dedner et al. 2002) for magnetic field divergence control (Split-Roe and Split-Bouchut), while others adopt unsplit time-stepping on a staggered mesh with an upwind version of Lee’s constrained transport scheme (D. Lee 2006) (USM-Roe, USM-HLLD, USM-HLLC, and USM-BK, where ‘USM’ stands for ‘unsplit-staggered mesh’). All our schemes use the 2nd-order TVD (total variation diminishing) interpolation of data in space and time using the Hancock method (B. Leer 1984). The details of the numerical schemes are summarized in Table 1.

4 BALSARA VORTEX

The Balsara vortex (D. S. Balsara 2004) is an exact stationary solution of the ideal MHD equations in two dimensions, where the centrifugal force, magnetic tension, thermal pressure gradient, and magnetic pressure gradient are perfectly balanced. This configuration, which conserves kinetic and magnetic energies independently in the absence of dissipative forces, serves as an excellent test problem for evaluating energy conservation in MHD simulations. Discretization errors and artificial discontinuities in finite-volume methods introduce numerical dissipation, leading to a loss of rotational and magnetic energy. Here we use the Balsara vortex to compare the energy conservation performance of various split and unsplit MHD solvers across different numerical schemes. While the dissipation we observe arises from a combination of numerical discretization and the choice of numerical technique (like reconstruction method, Riemann solver, etc.) as well as the presence of artificial discontinuities, we use the same resolution for all the different schemes in Table 1, such that we can compare the dissipation arising from the latter.

4.1 Initial conditions

The initial conditions for the Balsara vortex are given by

$$\mathbf{v} = \tilde{v} (-y\hat{\mathbf{x}} + x\hat{\mathbf{y}}) \exp\left(\frac{1-r^2}{2}\right), \quad (16)$$

$$\mathbf{B} = \tilde{B} (-y\hat{\mathbf{x}} + x\hat{\mathbf{y}}) \exp\left(\frac{1-r^2}{2}\right), \quad (17)$$

$$p_{\text{th}} = 1 + \left[\frac{\tilde{B}^2}{2}(1-r^2) - \frac{\tilde{v}^2}{2} \right] \exp(1-r^2), \quad (18)$$

$$\rho = 1, \quad (19)$$

where $r^2 = x^2 + y^2$, and $\hat{\mathbf{x}}$ and $\hat{\mathbf{y}}$ are unit vectors in the x and y directions, respectively. We use $\tilde{v} = 0.01$, $\tilde{B} = 0.01$, and $\gamma = 5/3$. Here we define the reference Mach number (\mathcal{M}) as the maximum local Mach number (M) in the simulation domain. Our choice

Table 1. Numerical schemes used in this work.

Scheme name (1)	Split/unsplit (2)	Riemann solver (3)	$\nabla \cdot \mathbf{B}$ Method (4)	Electric field reconstruction (5)
Split-Roe	Split	Roe	Dedner-Marder cleaning	N/A
Split-Bouchut	Split	Bouchut	Dedner-Marder cleaning	N/A
USM-Roe	Unsplit	Roe	Constrained transport	Lee-upwind
USM-HLLD	Unsplit	HLLD	Constrained transport	Lee-upwind
USM-HLLC	Unsplit	HLLC	Constrained transport	Lee-upwind
USM-BK	Unsplit	BK	Constrained transport	Lee-upwind

Note. Column (1): name of numerical scheme, (2): whether the scheme uses directionally split or unsplit updates, (3): Riemann solver—Roe (P. Roe 1981), Bouchut (K. Waagan et al. 2011), HLLD (T. Miyoshi & K. Kusano 2005), HLLC (S. Li 2005) or BK (C. Birke & C. Klingenberg 2023), (4): whether Dedner-Marder cleaning (B. Marder 1987; A. Dedner et al. 2002) or constrained transport (CT) (K. Yee 1966; C. R. Evans & J. F. Hawley 1988; W. Dai & P. R. Woodward 1998; T. A. Gardiner & J. M. Stone 2008) was used to handle the magnetic field divergence constraint, (5): Lee-upwind (D. Lee 2006) electric field reconstruction method, if applicable. All schemes use the 2nd-order Hancock (B. Leer 1984) method for interpolation of data in space and time.

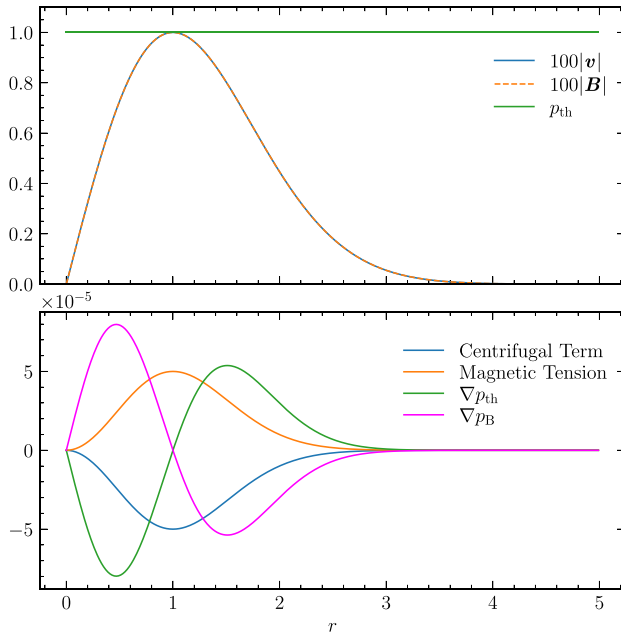


Figure 1. Top panel shows the radial profiles of velocity, magnetic field and pressure for the Balsara vortex, following equations (16)–(18) for a sonic Mach number of $\mathcal{M} = 0.01$ and the ratio of the magnetic to the rotational kinetic energy $\beta_1 = 1$. Note that the velocity and magnetic pressure profiles have been scaled by a factor of 100 for the sake of clarity. The scaled velocity profile touches the thermal pressure profile ($p_{\text{th}} \approx 1$) at $r = 1$ since $\mathcal{M} = 0.01$. The bottom panel shows that the centrifugal term $-(\mathbf{v} \cdot \nabla)\mathbf{v}$ is balanced by the magnetic tension $(\mathbf{B} \cdot \nabla)\mathbf{B}$, and the gradients of the thermal pressure (∇p_{th}) and the magnetic pressure (∇p_{B}) balance each other.

of parameters \tilde{v}, \tilde{B} and γ gives $\mathcal{M} \approx 0.01$. The radial profiles of velocity, magnetic field and pressure are shown in Fig. 1.

4.2 Set-up

We use a computational domain of $(x, y) \in [-5, 5] \times [-5, 5]$ and 64×64 grid cells with periodic boundary conditions and $M_{\text{cut}} = 0.02$ for our simulations. The problem is made computationally harder by advecting the vortex along the diagonal of the computational grid with speed \tilde{v} . We run our simulations for one complete advection of the vortex across the diagonal, such that it ends up exactly at the starting position, i.e. at the coordi-

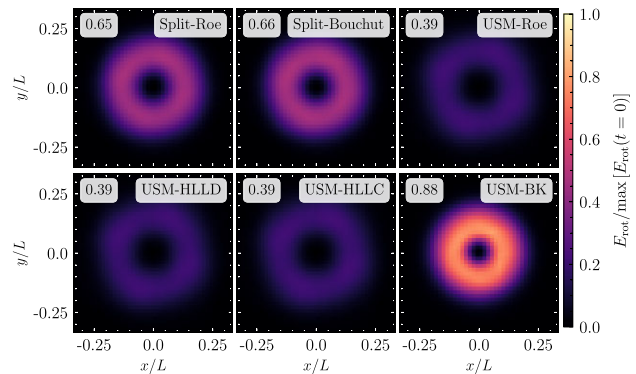


Figure 2. Rotational energy of the vortex after one advection diagonally through the computational domain for the six different numerical solver/scheme combinations (from left to right and top to bottom): Split-Roe, Split-Bouchut, USM-Roe, USM-HLLD, USM-HLLC, and USM-BK. The rotational energy has been normalized by the maximum rotational energy (at $r = 1$) at the beginning of the simulation ($t = 0$). The value in the top left corner of each panel shows the fraction of the total rotational energy left in the system compared to $t = 0$. We see that USM-BK outperforms all other schemes by retaining 88 per cent of the rotational kinetic energy.

nate origin. In this time interval, the vortex turns around 2.25 times.

4.3 Results and comparison of solvers

In order to quantify the amount of kinetic and magnetic energy dissipation, we calculate and compare the fraction of rotational and magnetic energy that the vortex has retained compared to their respective initial values. The rotational kinetic energy (E_{rot}) is calculated as

$$E_{\text{rot}} = \frac{1}{2} \rho \left[\left(v_x - \frac{\tilde{v}}{\sqrt{2}} \right)^2 + \left(v_y - \frac{\tilde{v}}{\sqrt{2}} \right)^2 \right], \quad (20)$$

while the magnetic energy (E_{mag}) is calculated as

$$E_{\text{mag}} = \frac{1}{2} |\mathbf{B}|^2. \quad (21)$$

Fig. 2 shows the fraction of the rotational energy retained in the system at the end of one complete advection of the vortex. The energy has been normalized by the maximum local rotational energy

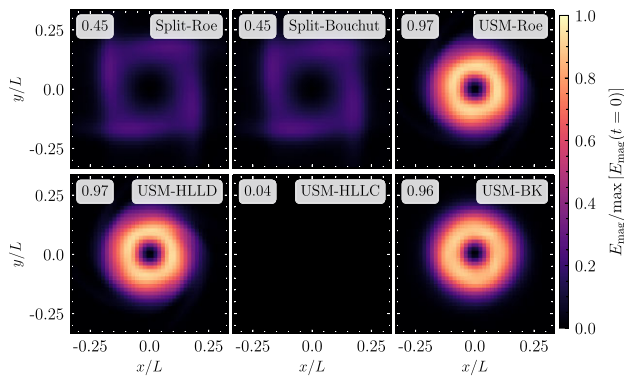


Figure 3. Same as Fig. 2, but for the magnetic energy. The value in the top left corner of each panel shows the fraction of the total magnetic energy left in the system after one complete box advection compared to $t = 0$. We find that the USM-BK scheme is also the best-performing scheme with respect to the magnetic energy, with only 4 per cent of the initial energy dissipated. The Split schemes dissipate magnetic energy while damping the magnetic monopoles, while the 3-wave USM-HLLC scheme has dissipated almost all of the magnetic energy in the system.

(at $r = 1$) present in the system at the beginning of the evolution. We find that the split schemes (Split-Roe and Split-Bouchut) retain around 65 per cent of the kinetic energy, while the unsplit schemes (USM), except for the USM-BK, retain only 39 per cent of the initial rotational kinetic energy. The new scheme (USM-BK; bottom right panel) performs the best, conserving 88 per cent of the rotational energy.

Fig. 3 shows the same as Fig. 2, but for the magnetic energy. Split-Roe and Split-Bouchut lose more than half of their initial magnetic energy and significantly distort the vortex into a nearly square-shaped form. The increased dissipation is a consequence of the divergence-cleaning method, which also dissipates magnetic energy while damping the magnetic monopoles. USM-Roe, USM-HLLD, and USM-BK perform similarly well in conserving the magnetic energy, with USM-BK retaining 96 per cent of the initial magnetic energy. At the same time, USM-HLLC, which considers only 3 waves in the Riemann solution, dissipates almost all the magnetic energy in the system. All schemes introduce minor distortions in the shape of the vortex. These are much more visible in the split schemes and USM-HLLC, but are minor in USM-Roe, USM-HLLD and USM-BK.

Finally, we look at the divergence of the magnetic field. We define a normalized version of $\nabla \cdot \mathbf{B}$, as

$$\nabla \cdot \hat{\mathbf{B}} = \nabla \cdot \frac{\mathbf{B} \Delta x}{B_{\text{rms}}}, \quad (22)$$

where B_{rms} is the root-mean-squared magnetic field integrated over the entire volume, and Δx is the side length of each grid cell. Fig. 4 shows $|\nabla \cdot \hat{\mathbf{B}}|$. The choice of Riemann solver does not play any significant role in constraining the divergence of the magnetic field to zero, however, all simulations using constrained transport (USM) perform much better compared to the divergence cleaning used in the split schemes. This is expected since divergence cleaning schemes do not enforce any particular discretization of $\nabla \cdot \mathbf{B}$ to zero. They instead rely on diffusing and damping numerical magnetic monopoles. On the other hand, constrained transport is designed such that $\nabla \cdot \mathbf{B} = 0$ to machine precision by the construction of a particular stencil chosen to construct \mathbf{B} from the electric field and to calculate $\nabla \cdot \mathbf{B}$.

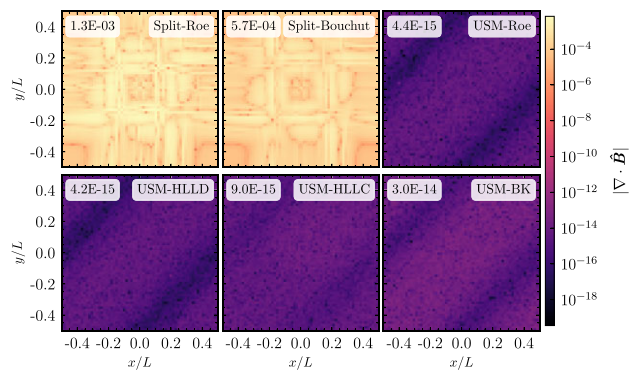


Figure 4. Same as Fig. 2, but for the divergence of the magnetic field, defined in a normalized fashion via equation (22), such that its magnitude can be compared to order unity. The inset on the top left in each panel shows the root-mean-squared value of $\nabla \cdot \hat{\mathbf{B}}$. The split schemes keep the value of $\nabla \cdot \mathbf{B}$ at reasonably low levels while the USM schemes maintain $\nabla \cdot \mathbf{B} = 0$ close to machine precision.

5 APPLICATION TO MAGNETIC FIELD AMPLIFICATION IN LOW-MACH TURBULENCE

5.1 Introduction to the turbulent dynamo

Magnetic fields play an important role in a wide variety of astrophysical systems, including accretion discs (R. F. Penna *et al.* 2010; Boneva, D. V. *et al.* 2021), star formation (A. R. Choudhuri 2015; C. Federrath 2015; P. Sharda *et al.* 2021), galaxies (A. A. Ruzmaikin, D. D. Sokolov & A. M. Shukurov 1988; R. Beck & R. Wielebinski 2013), and the interstellar medium (A. Fletcher *et al.* 2011; A. Seta & C. Federrath 2022). The presence of strong magnetic fields is attributed to the amplification of seed fields by *turbulent dynamos*. Turbulent dynamos amplify magnetic fields exponentially over short time-scales. This amplification is caused by a sequence of ‘stretching, twisting, folding, and merging’ (A. A. Schekochihin *et al.* 2004; A. Brandenburg & K. Subramanian 2005; C. Federrath 2016) of magnetic field lines induced by turbulent motions in the plasma, leading to an increase in the density of magnetic field lines in a fluid packet.

5.2 Numerical method and set-up

We solve equations (3)–(7) in a periodic 3D box of length L , uniformly discretized with a grid of 256^3 cells. Turbulence is driven stochastically by the Ornstein-Uhlenbeck process (V. Eswaran & S. B. Pope 1988; C. Federrath *et al.* 2010) implemented in the publicly available code TurbGen (C. Federrath *et al.* 2022). The turbulence driving field is constructed here to be purely solenoidal (divergence free), using a Helmholtz decomposition in Fourier space, where we measure wave numbers (k) in units of $2\pi/L$. The driving is constrained to large scales, i.e. $k = [1, 3]$, following a parabolic Fourier spectrum, where the peak injection is at $k_{\text{turb}} = 2$ and the driving amplitude falls off smoothly to zero at $k = 1$ and $k = 3$, respectively, as in previous works (e.g. C. Federrath *et al.* 2021). Using this turbulence driving method, we adjust the overall amplitude of the driver such that the turbulence reaches a target velocity dispersion $\sigma_v = \mathcal{M}c_s$ on scale $\ell_{\text{turb}} = L/k_{\text{turb}} = L/2$, where c_s is the sound speed and \mathcal{M} is the target turbulence Mach number. This defines

the turbulence turnover time-scale as $t_{\text{turb}} = \ell_{\text{turb}}/\sigma_v = L/(2\mathcal{M}c_s)$. Here, we study sonic Mach numbers of $\mathcal{M} = 0.1$ and 0.01 .

The box is initialized with a uniform density of fluid at rest and the sound speed is set to $c_s = 1$, i.e. all speeds are measured relative to the sound speed. The strength and statistical properties of the turbulent dynamo are independent of the structure of the initial magnetic field (A. Seta & C. Federrath 2020), so we initialize a uniform magnetic field in the z -direction of the computational domain to obtain a reference Alfvén Mach number of $\mathcal{M}_A = \sigma_v/c_A = 10^9$ when the turbulence is fully developed. This corresponds to a very weak initial seed field that is subsequently amplified by the turbulent dynamo.

Finally, for the runs with the USM-BK scheme, we set the cut-off Mach number (see equation 14) to $M_{\text{cut}} = \mathcal{M}$. Using $M_{\text{cut}}/\mathcal{M} = 1$ is acceptable for chaotic problems like turbulence, where, unlike the Balsara vortex, there is no strict structural symmetry to be preserved.

5.3 Results for Mach 0.1

In ideal-MHD, we set ν and η in equations (3)–(7) to 0. However, as shown earlier, numerical dissipation is always present owing to finite cell discretization (L. Malvadi Shivakumar & C. Federrath 2023) and due to the numerical scheme. Consequently, for excessively dissipative solvers, the results from numerical simulations can deviate significantly from the physical setting. In the following sections, we compare the effect of MHD solvers on the time evolution and morphology of the system and calculate the characteristic wave-numbers associated with numerical viscosity and resistivity at Mach 0.1. We run our simulations for a period of $100 t_{\text{turb}}$ to allow the magnetic field to saturate. However, we focus most of our analyses on the so-called ‘kinematic phase’, where the field does not have a strong back-reaction on the flow yet, and the field grows exponentially fast.

5.3.1 Time evolution

Fig. 5 shows the growth of the sonic Mach number (\mathcal{M}) in the top panel and the ratio of the magnetic energy to the kinetic energy ($E_{\text{mag}}/E_{\text{kin}}$) in the bottom panel. We see that the Mach number reaches the target value of 0.1 within $2 t_{\text{turb}}$. It is followed by the kinematic phase, where the magnetic energy increases exponentially (up to $10 - 30 t_{\text{turb}}$, depending on the numerical scheme used). This is attributed to the turbulent motions of the fluid, which stretch, twist, fold, and merge the magnetic field lines, leading to an increase in their concentration. Finally, as the magnetic field strength increases, the Lorentz force back-reacts on the turbulent motion, suppressing further amplification and saturating the magnetic field. This back-reaction also lowers the Mach number by about 20 per cent.

In order to measure the magnetic field dynamo growth rate, we fit the exponential model

$$\frac{E_{\text{mag}}}{E_{\text{kin}}} = Ae^{\Gamma t}, \quad (23)$$

in the kinematic phase, which we define as $5 \times 10^{-6} \leq E_{\text{mag}}/E_{\text{kin}} \leq 5 \times 10^{-3}$ (i.e. $E_{\text{mag}} \ll E_{\text{kin}}$), and Γ is the growth rate measured in units of t_{turb}^{-1} . The growth rates measured from the fits are listed in Table 2.

The USM-HLLC scheme exhibits an abnormally low growth rate. Consequently, the magnetic field and the Lorentz force is weaker compared to the other solvers and the sonic Mach number is higher. It also has a lower saturation level (see column 3 in Table 2). This behaviour is attributed to the excessive dissipation of magnetic energy by the HLLC solver (see bottom-middle panel in

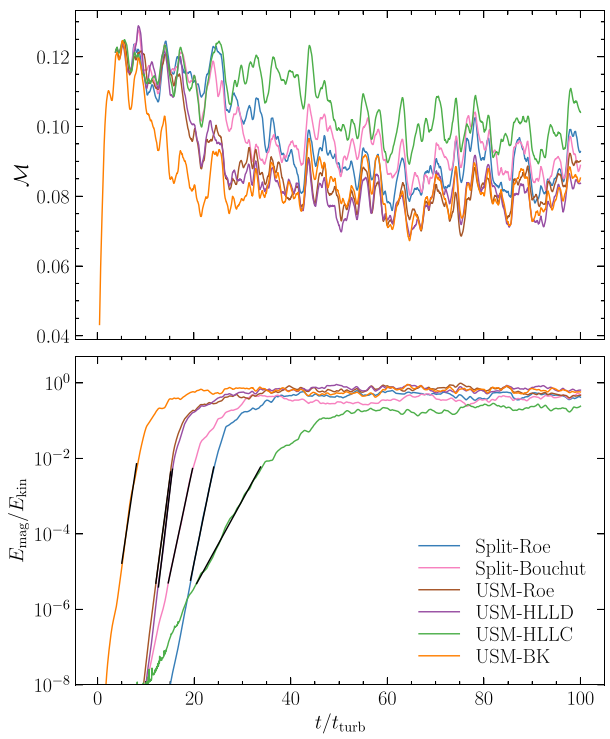


Figure 5. Time evolution of the sonic Mach number (top panel) and the ratio of magnetic to kinetic (turbulent) energy (bottom panel). The Mach number reaches the target value of ≈ 0.1 within $2 t_{\text{turb}}$, and during 3 and $10 - 30 t_{\text{turb}}$ (depending on the solver; labelled in the legend), the magnetic energy grows exponentially (see fitted solid lines in the bottom panel). Finally, once $E_{\text{mag}}/E_{\text{kin}} \gtrsim 0.5$, the field saturates and the growth stops, coinciding with a ≈ 20 per cent drop in the Mach number (see the top panel), due to the enhanced back-reaction of the field onto the flow. USM-HLLD, USM-Roe, and USM-BK have the highest growth rate (see Table 2) since they are less dissipative. On the other hand, the 3-wave USM-HLLC has the smallest growth rate, and it shows the weakest dip in Mach number owing to its excessive dissipation of the magnetic energy.

Fig. 3). In contrast, USM-HLLD, USM-Roe and USM-BK achieve the highest growth rates due to their reduced numerical dissipation. It is important to note that the growth rate depends on the magnetic Prandtl number (see C. Federrath et al. 2014), which, in turn, is determined by the ratio of the resistive to viscous dissipation wave-numbers (see Appendix B). Therefore, the growth rate is not a universal indicator of solver performance. For instance, USM-HLLD and USM-Roe simulations exhibit higher effective Prandtl numbers (see Table 5), resulting in a slightly higher growth rate than that of USM-BK.

5.3.2 Magnetic field structure

Numerical dissipation also affects the morphology of the system. To get a qualitative idea of this in turbulent flows, we investigate the spatial distribution of the magnetic energy. Fig. 6 shows a slice of the magnetic energy normalized by the mean magnetic energy during the kinematic phase of the dynamo, when $E_{\text{mag}}/E_{\text{kin}} = 10^{-4}$. We see random fluctuations in the magnetic energy field with all the solvers, however, the morphology is markedly different in USM-HLLC (bottom-middle panel) and slightly different for Split-Roe and Split-Bouchut (first two panels). They smear the over-densities and the under-densities in the field over larger regions. As mentioned

Table 2. Mach 0.1 turbulent dynamo measurements.

Name (1)	$\Gamma(t_{\text{turb}}^{-1})$ (2)	$(E_{\text{mag}}/E_{\text{kin}})_{\text{sat}}$ (3)	p_{bn} (4)	k_{bn} (5)	\tilde{k}_{ν} (6)	p_{ν} (7)	k_{ν} (8)	k_{η} (9)
Split-Roe	$1.43^{+0.01}_{-0.01}$	$0.48^{+0.07}_{-0.07}$	$0.92^{+0.09}_{-0.07}$	$5.5^{+0.3}_{-0.3}$	$5.9^{+0.1}_{-0.2}$	$1.0^{+0.1}_{-0.1}$	$6.3^{+0.1}_{-0.2}$	31^{+1}_{-1}
Split-Bouchut	$1.39^{+0.01}_{-0.01}$	$0.40^{+0.06}_{-0.06}$	$1.01^{+0.10}_{-0.08}$	$5.8^{+0.3}_{-0.3}$	$5.9^{+0.1}_{-0.2}$	$1.0^{+0.1}_{-0.1}$	$6.3^{+0.1}_{-0.2}$	31^{+1}_{-2}
USM-Roe	$2.20^{+0.01}_{-0.01}$	$0.66^{+0.13}_{-0.13}$	$0.42^{+0.28}_{-0.24}$	$4.0^{+0.8}_{-0.7}$	$6.8^{+1.7}_{-1.9}$	$1.0^{+0.1}_{-0.1}$	$6.4^{+0.6}_{-0.9}$	44^{+2}_{-1}
USM-HLLD	$2.48^{+0.01}_{-0.01}$	$0.69^{+0.09}_{-0.09}$	$0.35^{+0.35}_{-0.29}$	$3.9^{+0.7}_{-0.6}$	$7.1^{+2.2}_{-2.7}$	$1.0^{+0.1}_{-0.1}$	$6.5^{+0.6}_{-1.2}$	45^{+1}_{-2}
USM-HLLC	$0.54^{+0.01}_{-0.01}$	$0.21^{+0.04}_{-0.04}$	$0.36^{+0.38}_{-0.29}$	$4.1^{+1.0}_{-0.7}$	$7.4^{+2.1}_{-2.5}$	$1.1^{+0.1}_{-0.1}$	$6.5^{+0.7}_{-1.0}$	21^{+1}_{-2}
USM-BK	$2.00^{+0.01}_{-0.01}$	$0.58^{+0.10}_{-0.10}$	$-0.13^{+0.37}_{-0.30}$	$4.5^{+1.5}_{-1.0}$	$8.8^{+2.4}_{-2.8}$	$1.1^{+0.1}_{-0.1}$	$7.6^{+1.0}_{-1.1}$	40^{+1}_{-0}

Note. All parameters except the saturation value of the ratio of the magnetic energy to the kinetic energy (column 3) were measured/derived by averaging over the kinematic phase of the dynamo when $5 \times 10^{-6} \leq E_{\text{mag}}/E_{\text{kin}} \leq 5 \times 10^{-3}$. Columns: (1) Name of the numerical scheme as described in Table 1. (2) Growth rate in units of t_{turb}^{-1} . (3) Average value of the ratio of the magnetic energy to the kinetic energy in the saturation phase of the dynamo ($t > 60t_{\text{turb}}$). (4) Exponent of the bottleneck effect in the kinetic spectrum. (5) Scaling wave-number of the bottleneck effect. (6) Viscous dissipation wave-number if $p_{\nu} = 1$. (7) Exponent of the dissipation term of P_{kin} . (8) Viscous dissipation wave-number. (9) Resistive dissipation wave-number.

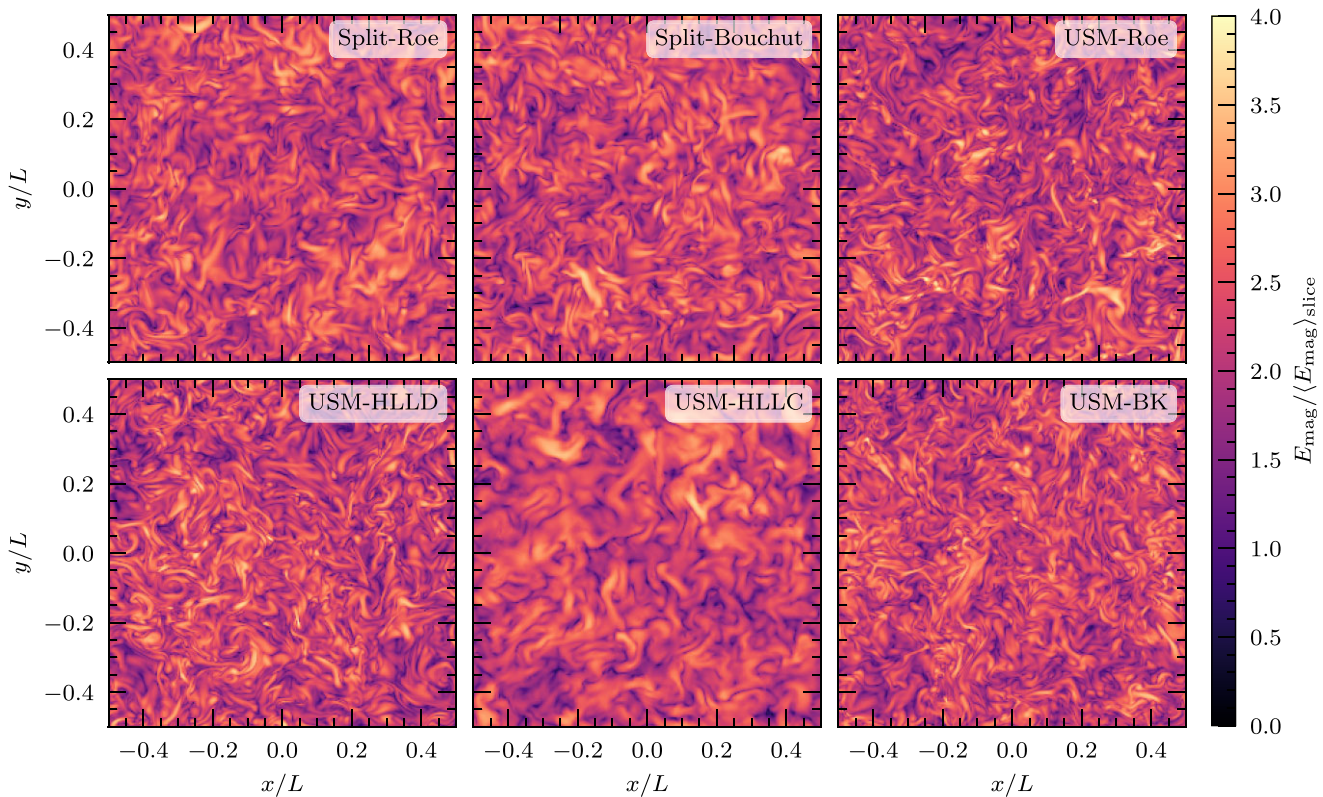


Figure 6. A slice of the magnetic energy normalized by the mean magnetic energy during the kinematic phase of the dynamo, when $E_{\text{mag}}/E_{\text{kin}} = 10^{-4}$, emphasizing its spatial distribution. The more dissipative Split schemes and USM-HLLC smear features over large-length scales while USM-Roe, USM-HLLD and USM-BK capture finer structures.

earlier, the dissipation in the Split schemes is attributed to divergence-cleaning, while that in USM-HLLC is a result of its consideration of fewer waves in the Riemann solution. In contrast, USM-HLLD and USM-BK display fine, small-scale structures. We quantitatively analyse the differences between the various schemes in the next section.

5.3.3 Spectral analysis

In subsonic turbulence, energy cascades from larger scales to smaller scales until it reaches a scale where it is dissipated due to the effects

of viscosity and resistivity (e.g. U. Frisch 1995). This takes place through the breaking-up of large eddies into smaller eddies. The wave-numbers where viscosity and resistivity act are called viscous dissipation wave-number k_{ν} , and resistive dissipation wave-number k_{η} , respectively.

We calculate the power spectrum of the kinetic energy averaged over the kinematic phase (as defined in Section 5.3.1) to measure the viscous dissipation wave-number. We follow the power spectrum model used in L. Malvadi Shivakumar & C. Federrath (2023) and fit the kinetic spectrum from $k \geq 3$ to exclude the turbulence driving scales. The upper limit of the fit is set to

$k_{\max} = N/8 = 32$, where N is the number of grid cells, to exclude spurious effects that arise on scales smaller than a few grid cells.

The kinetic energy power spectrum (P_{kin}) in the subsonic regime is modelled as

$$P_{\text{kin}}(k) = A_{\text{kin}} \left[\left(\frac{k}{k_{\text{bn}}} \right)^{-1.7} + \left(\frac{k}{k_{\text{bn}}} \right)^{p_{\text{bn}}} \right] \exp \left[- \left(\frac{k}{\tilde{k}_v} \right)^{p_v} \right], \quad (24)$$

where A_{kin} is the amplitude, k_{bn} is the scale of energy accumulation due to the bottleneck effect (G. Falkovich 1994; U. Frisch 1995; W. Schmidt, W. Hillebrandt & J. C. Niemeyer 2006; M. K. Verma & D. Donzis 2007), p_{bn} characterizes the strength of the bottleneck effect, and p_v characterizes the sharpness of the transition into dissipation. The viscous dissipation wave-number as defined in N. Kriel et al. (2022) is related to \tilde{k}_v and p_v by

$$k_v = \tilde{k}_v^{1/p_v}. \quad (25)$$

We point the reader to L. Malvadi Shivakumar & C. Federrath (2023) and references therein for the motivation behind this model.

To find the characteristic resistive dissipation wave-number (k_η), we follow the definition in N. Kriel et al. (2025), using the electric current ($\sim \nabla \times \mathbf{B}$) power spectrum. Since Ohmic dissipation is proportional to current, k_η is defined as the wave-number where the current attains a maximum.

The power spectra of kinetic energy, magnetic energy and current are shown in Fig. 7, and the fit parameters and the measured characteristic dissipation wave-numbers (k_v and k_η) are given in Table 2. For the kinetic spectra, the dissipation scales are similar for all solvers except USM-BK, which shows dissipation at larger wave-numbers (an ≈ 17 per cent difference compared to USM-HLLD). For the current spectra, we see that USM-HLLD marginally outperforms USM-BK (an ≈ 12 per cent difference). We also see that the dissipation scale for HLLC lies at very small wave-numbers, i.e. it induces numerical dissipation effects at much larger lengths scales, smearing out small-scale features. Thus, it is particularly unsuitable for modelling MHD flows.

5.3.4 Numerical Reynolds numbers

Since numerical dissipation is always present in MHD simulations, the simulated flows have a finite numerical hydrodynamic Reynolds number (Re) and magnetic Reynolds number (Rm), in contrast to a perfectly ideal setting, where these would be infinite, because $\nu = \eta = 0$ in the MHD equations. Appendix B describes the procedure for obtaining Re and Rm from the characteristic dissipation scales, using the key relations,

$$\text{Re} = \left(\frac{k_v}{c_{\text{Re}} k_{\text{driving}}} \right)^{4/3}, \quad (26)$$

$$\text{Pm} = \left(\frac{k_\eta}{c_{\text{Pm}} k_v} \right)^2, \text{ and} \quad (27)$$

$$\text{Rm} = \text{Re} \times \text{Pm}, \quad (28)$$

where $c_{\text{Re}} = 0.025^{+0.005}_{-0.006}$ and $c_{\text{Pm}} = 2.3^{+0.8}_{-0.5}$.

Table 3 lists the values of the effective Re , Rm , and Pm for the Mach 0.1 simulations, for each numerical scheme. The measured values of Re range between 630^{+290}_{-150} and 810^{+400}_{-240} (an ≈ 30 per cent variation), while Rm values vary between 1400^{+1200}_{-700} and 6300^{+5400}_{-3000} (a striking ≈ 350 per cent variation attributable to the choice of the numerical scheme). The Pm values (which can be calculated from Re and Rm) vary between $2.1^{+1.6}_{-1.0}$ and $9.9^{+7.0}_{-4.6}$ (an ≈ 370 per cent

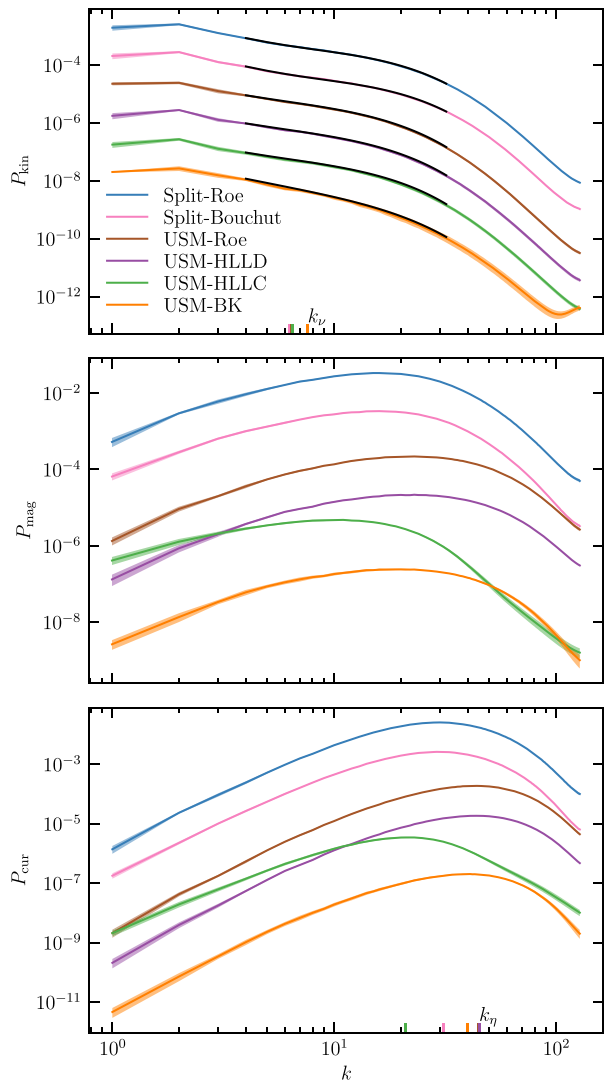


Figure 7. Time-averaged kinetic power spectra (top panel), magnetic power spectra (middle panel), and current power spectra (bottom panel) for various solvers. The spectra are multiplied for every solver except Split-Roe by a factor of 0.1 relative to the next solver in the legends. The black lines in the kinetic power spectra are the fits to the model given in equation (24). The viscous dissipation scale and resistive dissipation scale are marked on the x -axis. The viscous dissipation scales are clustered around each other for all solvers; however, the resistive dissipation scale measurements clearly show that HLLC is not suitable for MHD simulations since it is dissipative at very large length scales.

Table 3. Mach 0.1 turbulent dynamo effective Reynolds numbers.

Name (1)	Re (2)	Rm (3)	Pm (4)
Split-Roe	$6.3^{+2.9}_{-1.5} \times 10^2$	$3.0^{+2.5}_{-1.5} \times 10^3$	$4.7^{+2.9}_{-2.2}$
Split-Bouchut	$6.4^{+2.7}_{-1.5} \times 10^2$	$3.0^{+2.5}_{-1.4} \times 10^3$	$4.6^{+2.9}_{-2.0}$
USM-Roe	$6.4^{+2.9}_{-1.8} \times 10^2$	$6.3^{+5.4}_{-3.0} \times 10^3$	$9.9^{+7.0}_{-4.6}$
USM-HLLD	$6.4^{+3.3}_{-2.0} \times 10^2$	$6.1^{+5.1}_{-3.0} \times 10^3$	$9.4^{+7.3}_{-4.4}$
USM-HLLC	$6.5^{+3.2}_{-1.9} \times 10^2$	$1.4^{+1.2}_{-0.7} \times 10^3$	$2.1^{+1.6}_{-1.0}$
USM-BK	$8.1^{+4.0}_{-2.4} \times 10^2$	$4.6^{+3.7}_{-2.2} \times 10^3$	$5.6^{+4.2}_{-2.6}$

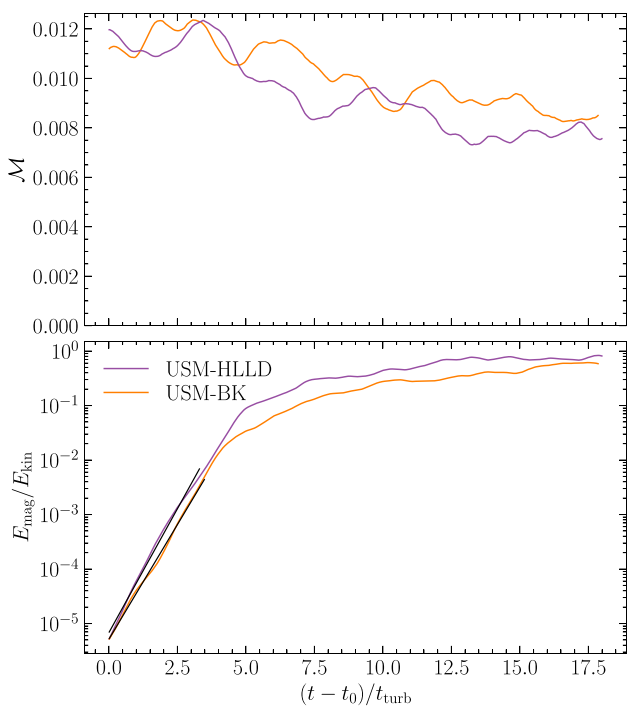


Figure 8. Similar to Fig. 5, but for Mach 0.01, comparing the best-performing solvers from the previous comparison at Mach 0.1, namely USM-BK and USM-HLLD. Note that the x -axis shows $(t - t_0)/t_{\text{turb}}$, where t_0 is chosen such that both runs start at the same $E_{\text{mag}}/E_{\text{kin}}$ to facilitate the comparison.

variation). We see that the USM-BK scheme shows the highest Re (810^{+400}_{-240} compared to 640^{+330}_{-200} for USM-HLLD, the next-highest value). This suggests that USM-BK has the least dissipation of kinetic energy in the low-Mach regime among the solvers/schemes compared; however, the large error bars show that the difference between the dissipation properties of the USM-HLLD and USM-BK is not statistically significant at Mach 0.1. We further find that USM-HLLD and USM-Roe have a higher Pm than USM-BK ($9.4^{+7.3}_{-4.4}$ and $9.9^{+7.0}_{-4.6}$ for USM-HLLD and USM-BK, respectively, compared to $5.6^{+4.2}_{-2.6}$ for USM-BK). As the dynamo growth rate depends on Re as well as Pm (see C. Federrath et al. 2014), these measurements of Pm explain why USM-BK has a somewhat smaller growth rate (c.f., Fig. 5 and Table 2) compared to USM-HLLD, despite being the least dissipative solver.

5.4 Results for Mach 0.01

We have already established in the Balsara vortex test (c.f., Section 4) that the schemes using Dedner-Marder cleaning do not perform very well in constraining the divergence of the magnetic field to zero. From our analysis of the electric current power spectra, it

Table 5. Same as Table 3, but for Mach 0.01.

Name (1)	Re (2)	Rm (3)	Pm (4)
USM-HLLD	$2.4^{+1.4}_{-0.8} \times 10^2$	$5.5^{+6.8}_{-3.1} \times 10^3$	21^{+31}_{-12}
USM-BK	$8.0^{+3.8}_{-2.2} \times 10^2$	$5.2^{+5.7}_{-2.7} \times 10^3$	$6.5^{+6.1}_{-3.3}$

is quite clear that HLLC is not suitable for low-Mach simulations due to its large resistive dissipation length scale. Based on our study of energy conservation and the current power spectra, we can conclude that USM-HLLD and USM-BK have been the best-performing solvers so far, showing comparable results. Given that many astrophysical processes, such as stratified stellar flows (see F. Kupka & H. J. Muthsam 2017) and early-Universe turbulent dynamos (see R. Achikanath Chirakkara et al. 2021), involve highly subsonic flows with Mach numbers below 10^{-2} , we test these schemes further by running a turbulent dynamo simulation at Mach 0.01. Since our focus is on the kinematic stage of the dynamo (which we use to obtain solver properties), we stop our simulations close to the onset of saturation.

5.4.1 Time evolution

Fig. 8 shows the evolution of the Mach number and the ratio of magnetic energy to kinetic energy with time. The plots have been shifted so that both simulations have the same starting ratio of the kinetic energy to the magnetic energy, facilitating the comparison, as the initial conditions are not relevant for the turbulent dynamo (A. Seta & C. Federrath 2020; J. R. Beattie et al. 2023). The features are similar to what we see at Mach 0.1 (cf., Fig. 5). We define the kinematic phase as in Section 5.3.1 ($5 \times 10^{-6} \leq E_{\text{mag}}/E_{\text{kin}} \leq 5 \times 10^{-3}$), with the measured growth rate listed in Table 4. The growth rate is slightly higher for USM-HLLD compared to USM-BK, which is consistent with the higher Prandtl number of USM-HLLD (see Table 5), similar to what we found for the Mach 0.1 comparison of the two solvers.

5.4.2 Morphology

Fig. 9 shows the kinetic energy, the magnetic energy, and the vorticity, respectively, in a slice during the kinematic phase when $E_{\text{mag}}/E_{\text{kin}} = 10^{-4}$. We see that more small-scale kinetic structure is captured in USM-BK compared to USM-HLLD. This is consistent with the fact that USM-BK dissipates kinetic energy at smaller length scales compared to USM-HLLD. The presence of small-scale structures (left panel) shows that smaller eddies are present in the USM-BK test case, whereas USM-HLLD dissipates energy into heat before forming eddies of comparable sizes. A similar pattern is hinted by the magnetic energy (middle panel), where USM-BK captures somewhat more small-scale structure than USM-HLLD.

Table 4. Same as Table 2, but for Mach 0.01.

Name (1)	$\Gamma(t_{\text{turb}}^{-1})$ (2)	p_{bn} (3)	k_{bn} (4)	\tilde{k}_v (5)	p_v (6)	k_v (7)	k_η (8)
USM-HLLD	$2.09^{+0.02}_{-0.02}$	$0.3^{+0.2}_{-0.2}$	$2.0^{+0.7}_{-0.4}$	$2.6^{+0.8}_{-0.6}$	$0.8^{+0.1}_{-0.1}$	$3.1^{+0.8}_{-0.7}$	31^{+9}_{-6}
USM-BK	$1.94^{+0.01}_{-0.01}$	$-0.2^{+0.2}_{-0.2}$	$4.7^{+0.5}_{-0.5}$	$10.6^{+1.4}_{-1.4}$	$1.2^{+0.1}_{-0.1}$	$7.4^{+1.0}_{-0.6}$	40^{+5}_{-3}

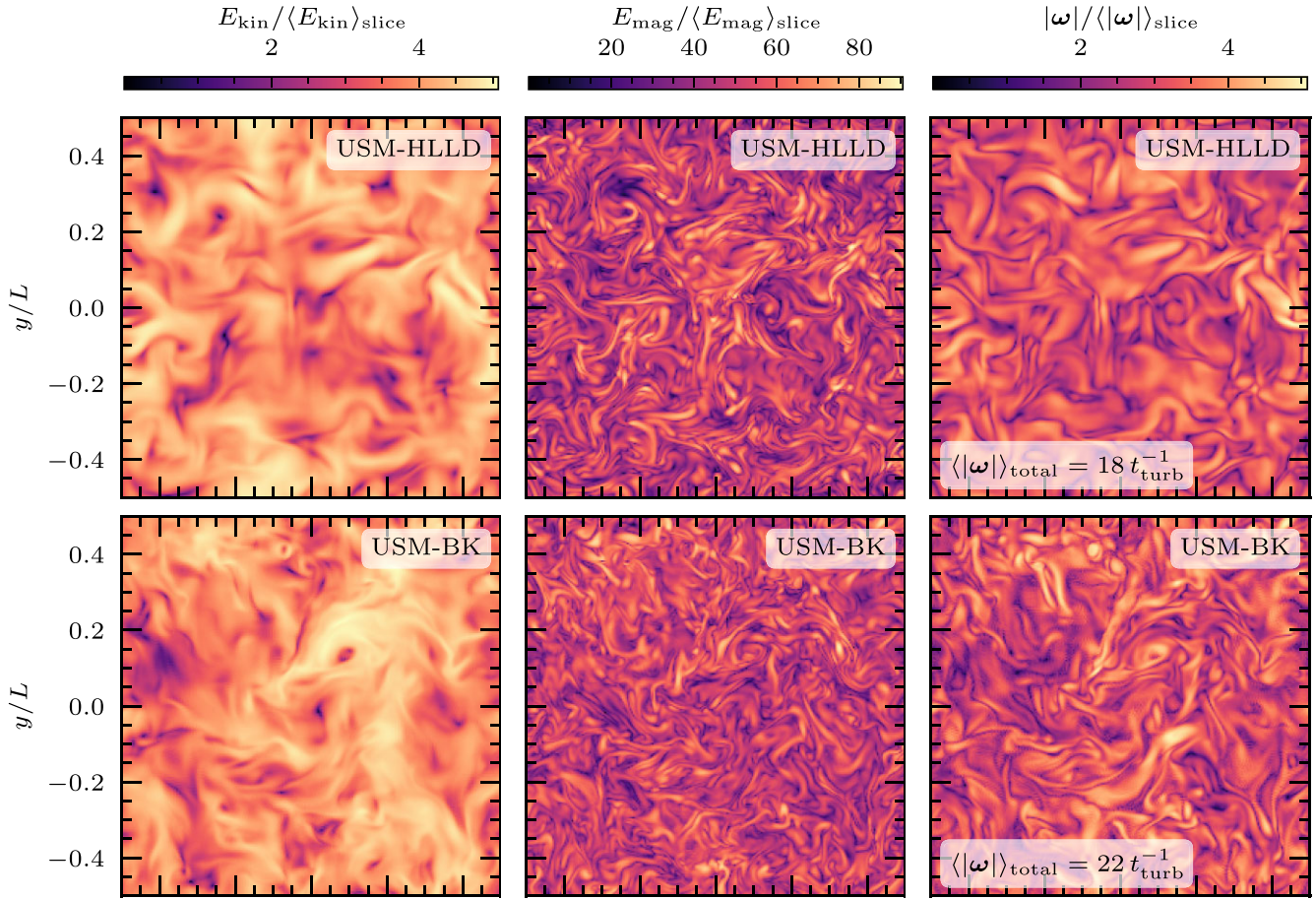


Figure 9. Slices of kinetic energy (left), magnetic energy (middle), and vorticity, $\omega = \nabla \times \mathbf{v}$ (right), through the simulation domain taken during the kinematic phase of the turbulent dynamo at Mach 0.01 when $E_{\text{mag}}/E_{\text{kin}} = 10^{-4}$. The presence of small-scale structure in USM-BK shows that it dissipates kinetic energy at smaller length scales compared to USM-HLLD. Compared to the kinetic energy, the magnetic energy (middle panels) shows somewhat smaller qualitative differences between the two solvers, but it appears that also here the USM-BK captures slightly more small-scale turbulent structure than USM-HLLD. Finally, the vorticity (right-hand panels) reinforces the finding that USM-BK captures more small-scale structure than USM-HLLD. The inset labels on the vorticity panels show measurements of the mean vorticity in the entire system (not just the slice), demonstrating that USM-BK captures ~ 20 per cent more vorticity than USM-HLLD.

This difference is demonstrated quantitatively in the next section. Our findings are further corroborated by the vorticity modulus (right panel), where USM-BK captures ~ 20 per cent more vorticity (see inset label) than USM-HLLD.

5.4.3 Spectral analysis

We repeat the analysis in Section 5.3.3 for the two Mach 0.01 runs. Fig. 10 shows the kinetic energy, magnetic energy, current, and vorticity power spectra. The kinetic spectra reveal that USM-HLLD turns downwards (a sign of the onset of dissipation) on scales larger (wave-numbers smaller) than USM-BK, implying that USM-BK dissipates kinetic energy at smaller length scales compared to USM-HLLD, and is therefore less dissipative. The current power spectrum peaks at a larger wave-number for USM-BK than USM-HLLD, implying that magnetic resistivity starts acting at smaller length scales for USM-HLLD compared to USM-BK, i.e. USM-HLLD is somewhat more resistive than USM-BK. The sharp downward turn of the vorticity power spectrum of USM-HLLD indicates that smaller eddies have been dissipated into heat, a consequence of smaller viscous dissipations wave-number. The fitted dissipation wave-numbers are

reported in Table 4. We find that USM-BK dissipates at significantly smaller length scales both in terms of kinetics (58 per cent difference in the wave-numbers) and magnetics (23 per cent difference in the wave-numbers).

5.4.4 Numerical Reynolds numbers

Following the relations given in Appendix B, we measure the numerical hydrodynamic and magnetic Reynolds numbers, and the Prandtl number in Table 5. We find that USM-BK has $\text{Re} = 800_{-220}^{+380}$, while USM-HLLD has $\text{Re} = 240_{-80}^{+140}$, implying that the former is less dissipative. We note that the Re for USM-HLLD has dropped by a factor of 2.5, compared to the Mach 0.1 run, while USM-BK has roughly the same value, demonstrating that the solver successfully retains high values of Re even at low Mach number. The Pm for USM-BK is lower ($\text{Pm} = 6.5_{-3.3}^{+6.1}$) compared to USM-HLLD ($\text{Pm} = 21_{-12}^{+31}$), which explains why USM-BK has a lower growth rate in Table 4. Since Pm is so much higher in USM-HLLD, the product of Re and Pm , i.e. Rm , turns out to be similar for both solvers.

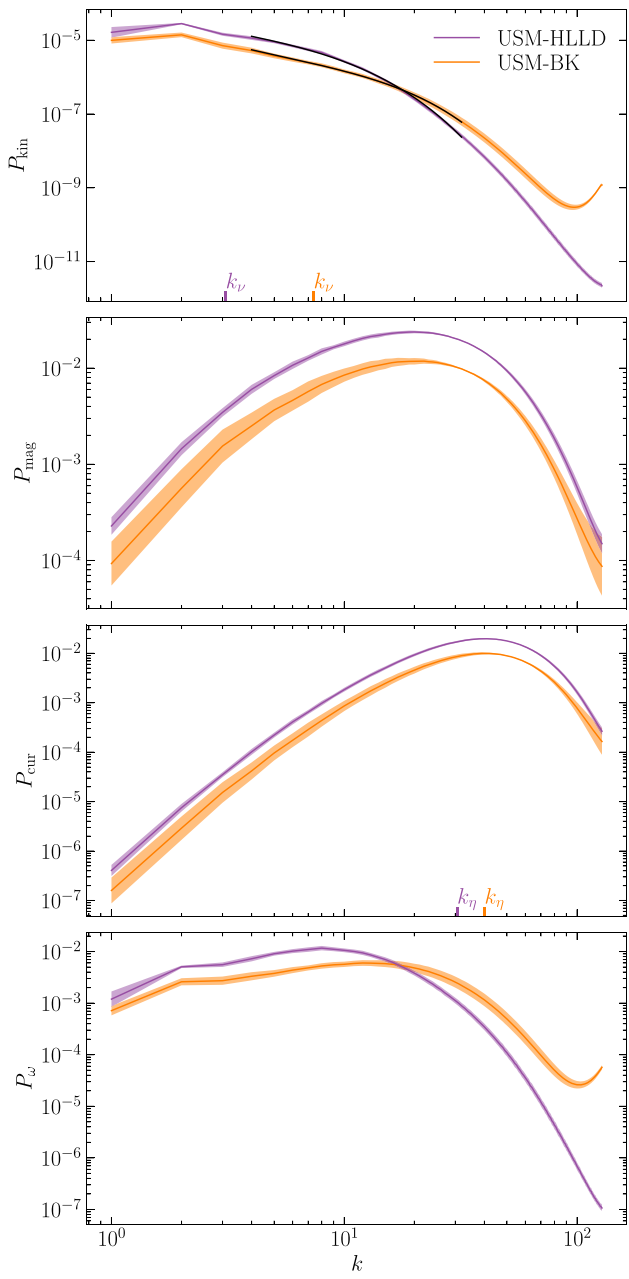


Figure 10. Time-averaged power spectra of the kinetic energy (top panel), magnetic energy (second panel), electric current (third panel) and vorticity (bottom panel), for USM-HLLD and USM-BK. USM-BK has been shifted by a factor of 0.5 along the y-axis for clarity. The black lines are the fits to the model given in equation (24). The viscous dissipation scale and resistive dissipation scale are marked on the x-axis. Both the viscous and resistive dissipation scales are significantly separated from each other, showing that USM-BK is less dissipative than USM-HLLD, in both kinetics and magnetics.

5.5 Computational cost

Factoring out the sound speed (c_s) in equation (13) and approximating the Alfvén speed in the x -direction by the total Alfvén speed ($c_{A,x} \approx c_A$), we can write the fastest wave-speed as

$$\lambda_{\text{fastest}} \approx c_s M + \frac{c_s}{2} \sqrt{\left(\frac{1}{M_{\text{BK}}^2} + \frac{M^2}{M_A^2} \right) + \sqrt{\left(\frac{1}{M_{\text{BK}}^2} + \frac{M^2}{M_A^2} \right)^2 - 4 \frac{M^2}{M_A^2}}}, \quad (29)$$

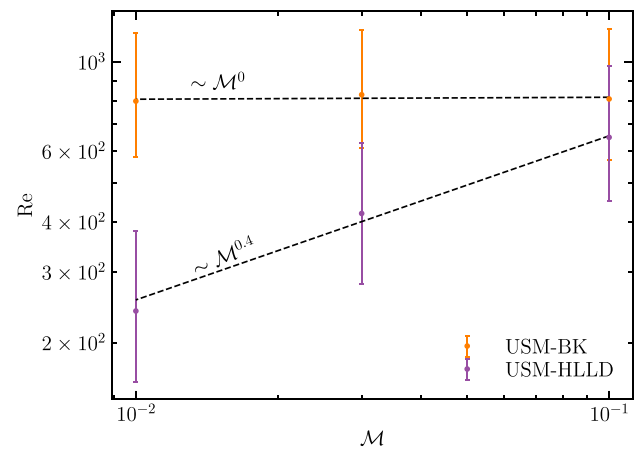


Figure 11. The effective numerical hydrodynamic Reynolds number (Re) as a function of the turbulent Mach number (\mathcal{M}). Re does not change with \mathcal{M} for USM-BK; however, it decreases with decreasing Mach number for USM-HLLD.

where $M_{\text{BK}} = 1$ for conventional Riemann solvers, while $M_{\text{BK}} \approx \mathcal{M}$ for the BK method, for our choice of $M_{\text{cut}} = \mathcal{M}$. For our application of turbulent dynamos where $M \approx \mathcal{M} \ll 1 \ll \mathcal{M}_A \approx M_A$ and $c_s \approx 1$, this can be written as

$$\lambda_{\text{fastest}} \sim \mathcal{M} + \frac{1}{M_{\text{BK}}}. \quad (30)$$

We can immediately see that for conventional Riemann solvers, the fastest signal speed scales as $(1 + \mathcal{M}) \sim 1$ while for the BK method it scales as $\sim 1/\mathcal{M}$. Therefore, the time-step ($\Delta t \propto c_{\text{fastest}}^{-1}$) is independent of the Mach number for conventional solvers, however, $\Delta t \propto \mathcal{M}$ for the BK method (see equation 15).

Since the turbulent turnover time (t_{turb}) also scales as $\sim 1/\mathcal{M}$ (c.f., Section 5.2), the number of time-steps required to achieve the same amount of time evolution (i.e. the number of eddy-turnover times of evolution) also scales as $\sim 1/\mathcal{M}$. Therefore, the total cost of a simulation with the BK method scales as $1/\mathcal{M}^2$, while that for conventional Riemann solvers goes as $1/\mathcal{M}$. If the end goal is to achieve the highest numerical Re possible, either USM-BK can be used at some resolution or USM-HLLD can be used at a comparatively higher resolution. Fig. 11 shows the variation of numerical Re with \mathcal{M} at fixed resolution (N). For USM-BK, Re does not change significantly with \mathcal{M} ; however, it scales as $\mathcal{M}^{0.4}$ for USM-HLLD. L. Malvadi Shivakumar & C. Federrath (2023) have shown that the effective numerical Re varies as $N^{4/3}$, where N is the number of grid cells in each direction.

Therefore, for a given Mach number and resolution, the effective Re for the two solvers goes as

$$\begin{aligned} \text{Re}_{\text{BK}} &\sim \mathcal{M}^0 N^{4/3}, \\ \text{Re}_{\text{HLLD}} &\sim \mathcal{M}^{0.4} N^{4/3}. \end{aligned} \quad (31)$$

The ratio of computational cost (\mathcal{C}) for the two solvers at a given Mach number and resolution is given by

$$\frac{\mathcal{C}_{\text{BK}}}{\mathcal{C}_{\text{HLLD}}} \sim \frac{\mathcal{M}^{-2} N^4}{\mathcal{M}^{-1} N^4}. \quad (32)$$

To achieve a target $\text{Re} = \text{Re}_{\text{BK}} = \text{Re}_{\text{HLLD}}$ at a fixed Mach number by varying the resolution, we can use equations (31) and (32), and

write the ratio of the computational cost as

$$\frac{C_{BK}}{C_{HLLD}} \sim \frac{\mathcal{M}^{-2} \text{Re}^3}{\mathcal{M}^{-1} \mathcal{M}^{-1.2} \text{Re}^3} \sim \mathcal{M}^{0.2}. \quad (33)$$

Thus, we can say that USM-BK is marginally better than USM-HLLD on the metric of computational cost. An implicit implementation of the BK method, which is less restrictive in the time-step constraint is preferable and we leave it to future works.

6 CONCLUSIONS

We examined the impact of numerical schemes, particularly the choice of Riemann solver, on numerical dissipation in low-Mach MHD simulations. Using the Balsara vortex test problem, we assessed the suitability of the new Riemann solver (USM-BK) and explored its effectiveness in capturing structures in low-Mach turbulent dynamo simulations. The following are the main conclusions drawn from this work:

- (i) Conventional Riemann solvers (Roe, HLLC, HLLD, and Bouchut) exhibit excessive dissipation in the low-Mach regime.
- (ii) The new USM-BK solver demonstrates the least dissipation of kinetic energy in the Balsara vortex tests at Mach 0.01, preserving 84 per cent of the kinetic energy after one complete advection of the vortex across the computational grid. In contrast, USM-Roe, USM-HLLC, and USM-HLLD show the highest dissipation, preserving only 39 per cent of the kinetic energy.
- (iii) The USM-BK solver also exhibits very little dissipation of magnetic energy at Mach 0.01, retaining 96 per cent of the magnetic energy after one complete advection of the Balsara vortex. It is marginally outperformed by USM-HLLD and USM-Roe, which retain 97 per cent of the magnetic energy.
- (iv) An unsplit-staggered mesh (USM) implementation of the BK Riemann solver is preferred over the usage of divergence cleaning since divergence cleaning also diffuses the magnetic energy. Furthermore, constrained transport keeps the divergence of magnetic field close to zero up to machine precision, by construction.
- (v) The time-step restriction for stability for USM-BK scales as $\Delta t \sim O(\mathcal{M})$ (c.f., equation 15). Therefore, implicit time-steppers are preferable for applications in the low Mach regime.
- (vi) As discussed in Section 5, the choice of Riemann solver significantly influences both the growth rate and the saturation level of the dynamo due to variations in the effective Reynolds numbers between solvers. We measured the growth rates and the corresponding effective Reynolds numbers for various solvers at Mach 0.1 and Mach 0.01.
- (vii) The new solver can resolve smaller length scales compared to the other solvers, which is evident from the kinetic and electric current spectra. While USM-HLLD marginally outperforms USM-BK in resolving magnetic structures at Mach 0.1, USM-BK surpasses USM-HLLD in performance as the Mach number is decreased. This difference in dissipation length scales is also reflected in the morphological features seen in snapshots taken during the kinematic phase.
- (viii) At a given energy ratio, USM-BK captures more vorticity compared to USM-HLLD. The vorticity power spectra show that USM-BK has more power at smaller wave-numbers than USM-HLLD, indicating that USM-BK captures more small-scale structures since smaller eddies have not been dissipated into heat.

We conclude that the new USM-BK solver is the most suitable for low-Mach MHD simulations, among the schemes compared, as

it exhibits the least dissipation of kinetic and magnetic energy. The solver is particularly effective in capturing small-scale structures of the flow, making it a good choice for turbulent dynamo simulations in the low-Mach regime.

ACKNOWLEDGEMENTS

We thank Knut Waagan and Dinshaw Balsara for helpful discussions. C. F. acknowledges funding provided by the Australian Research Council (Discovery Project grants DP230102280 and DP250101526), and the Australia-Germany Joint Research Cooperation Scheme (UA-DAAD). We further acknowledge high-performance computing resources provided by the Leibniz Rechenzentrum and the Gauss Centre for Supercomputing (grants pr32lo, pr48pi, pn76ga and GCS Large-scale project 10391), the Australian National Computational Infrastructure (grant ek9) and the Pawsey Supercomputing Centre (project pawsey 0810) in the framework of the National Computational Merit Allocation Scheme and the ANU Merit Allocation Scheme. The simulation software, FLASH, was in part developed by the Flash Centre for Computational Science at the University of Chicago and the Department of Physics and Astronomy at the University of Rochester. We also acknowledge the use of OpenAI's ChatGPT for assistance in proofreading and improving the clarity of the manuscript, and GitHub Copilot for assistance in generating code.

DATA AVAILABILITY

The data used in this article (approximately 4 TB) is available upon reasonable request to the authors.

REFERENCES

- Achikanath Chirakkara R., Federrath C., Trivedi P., Banerjee R., 2021, *Phys. Rev. Lett.*, 126, 091103
- Balsara D. S., 2004, *ApJS*, 151, 149
- Beattie J. R., Federrath C., Kriel N., Mocz P., Seta A., 2023, *MNRAS*, 524, 3201
- Beck R., Wielebinski R., 2013, Magnetic Fields in Galaxies. Springer Netherlands, Dordrecht, p. 641, https://doi.org/10.1007/978-94-007-5612-0_13
- Berger M. J., Colella P., 1989, *J. Comput. Phys.*, 82, 64
- Birke C., Klingenberg C., 2023, in Franck E., Fuhrmann J., Michel-Dansac V., Navoret L., eds, A Low Mach Number Two-Speed Relaxation Scheme for Ideal MHD Equations, Finite Volumes for Complex Applications X—Volume 2, Hyperbolic and Related Problems, . Springer Nature, Switzerland, Cham, p. 43
- Birke C., Chalons C., Klingenberg C., 2023, *Commun. Math. Sci.*, 21, 2213
- Birke C., Boscheri W., Klingenberg C., 2024, *J. Sci. Comput.*, 98, 34, preprint ([arXiv:2306.16286](https://arxiv.org/abs/2306.16286))
- Boneva D. V., Mikhailov E. A., Pashentseva M. V., Sokoloff D. D., 2021, *A&A*, 652, A38
- Boscheri W., Thomann A., 2024, A structure-preserving semi-implicit IMEX finite volume scheme for ideal magnetohydrodynamics at all Mach and Alfvén numbers, preprint ([arXiv:2403.04517](https://arxiv.org/abs/2403.04517)), <https://arxiv.org/abs/2403.04517>
- Brandenburg A., Subramanian K., 2005, *Phys. Rep.*, 417, 1
- Chen W., Wu K., Xiong T., 2023, *J. Comput. Phys.*, 488, 112240
- Choudhuri A. R., 2015, Natures's Third Cycle: A Story of Sunspots. Oxford
- Clerc S., 2000, *J. Comput. Phys.*, 161, 354
- Dai W., Woodward P. R., 1998, *ApJ*, 494, 317
- Dedner A., Kemm F., Kröner D., Munz C. D., Schnitzer T., Wesenberg M., 2002, *J. Comput. Phys.*, 175, 645
- Dubey A. et al., 2008, in Pogorelov N. V., Audit E., Zank G. P. eds, ASP Conf. Ser. Vol. 385, Numerical Modeling of Space Plasma Flows. Astron. Soc. Pac., San Francisco, p. 145

Dumbser M., Balsara D., Tavelli M., Fambri F., 2018, *Int. J. Num. Methods Fluids*, 89, 16

Eswaran V., Pope S. B., 1988, *Comput. Fluids*, 16, 257

Evans C. R., Hawley J. F., 1988, *ApJ*, 332, 659

Falkovich G., 1994, *Physics of Fluids*, 6, 1411

Fambri F., 2021, *Int. J. Num. Methods Fluids*, 93, 3447

Fambri F., Sonnendrücker E., 2024, Structure Preserving Hybrid Finite Volume Finite Element Method for Compressible MHD, preprint (arXiv:2407.14141), <https://arxiv.org/abs/2407.14141>

Federrath C., 2015, *MNRAS*, 450, 4035

Federrath C., 2016, *J. Plasma Phys.*, 82, 535820601

Federrath C., Roman-Duval J., Klessen R. S., Schmidt W., Mac Low M. M., 2010, *A&A*, 512, A81

Federrath C., Schober J., Bovino S., Schleicher D. R. G., 2014, *ApJ*, 797, L19

Federrath C., Klessen R. S., Iapichino L., Beattie J. R., 2021, *Nat. Astron.*, 5, 365

Federrath C., Roman-Duval J., Klessen R. S., Schmidt W., Mac Low M. M., 2022, Astrophysics Source Code Library, record ascl:2204.001

Fletcher A., Beck R., Shukurov A., Berkhuijsen E. M., Horellou C., 2011, *MNRAS*, 412, 2396

Frisch U., 1995, *Turbulence the Legacy of A. N. Kolmogorov*. Cambridge Univ. Press, Cambridge

Fryxell B. et al., 2000, *ApJS*, 131, 273

Gardiner T. A., Stone J. M., 2008, *J. Comput. Phys.*, 227, 4123

Guillard H., Murrone A., 2004, *Comput. Fluids*, 33, 655

Klein R., 1995, *J. Comput. Phys.*, 121, 213

Kriel N., Beattie J. R., Seta A., Federrath C., 2022, *MNRAS*, 513, 2457

Kriel N., Beattie J. R., Federrath C., Krumholz M. R., Hew J. K. J., 2025, *MNRAS*, 534, 2602

Kupka F., Muthsam H. J., 2017, *Living Rev. Comput. Astrophys.*, 3, 1

Lee D., 2006, PhD thesis, University of Maryland, <http://hdl.handle.net/1903/3842>

van Leer B., 1984, *SIAM J. Sci. Stat. Comput.*, 5, 1

Leggett J., Zhao Y., Sandberg R. D., 2022, *J. Turbomachinery*, 145, 011002

Leidi G., Birke C., Andrassy R., Higl J., Edelmann P. V. F., Wiest G., Klingenberg C., Röpke F. K., 2022, *A&A*, 668, A143

Li S., 2005, *J. Comput. Phys.*, 203, 344

Malvadi Shivakumar L., Federrath C., 2023, preprint (arXiv:2311.10350)

Marder B., 1987, *J. Comput. Phys.*, 68, 48

Miczek F., Röpke F. K., Edelmann P. V. F., 2015, *A&A*, 576, A50

Min M. et al., 2024, preprint (arXiv:2409.19119)

Minoshima T., Miyoshi T., 2021, *J. Comput. Phys.*, 446, 110639

Miyoshi T., Kusano K., 2005, *J. Comput. Phys.*, 208, 315

Park H., Linton D., Thorner B., 2022, *Int. J. Heat Fluid Flow*, 93, 108916

Penna R. F., McKinney J. C., Narayan R., Tchekhovskoy A., Shafee R., McClintock J. E., 2010, *MNRAS*, 408, 752

Roe P., 1981, *J. Comput. Phys.*, 43, 357

Ruzmaikin A. A., Sokolov D. D., Shukurov A. M., 1988, *Magnetic Fields of Galaxies. Astrophysics and Space Science Library Vol. 133*, Springer Dordrecht

Schekochihin A. A., Cowley S. C., Maron J. L., McWilliams J. C., 2004, *Phys. Rev. Lett.*, 92, 054502

Schmidt W., Hillebrandt W., Niemeyer J. C., 2006, *Comput. & Fluids*, 35, 353, preprint (astro-ph/0407616)

Seta A., Federrath C., 2020, *MNRAS*, 499, 2076

Seta A., Federrath C., 2022, *MNRAS*, 514, 957

Sharda P., Federrath C., Krumholz M. R., Schleicher D. R. G., 2021, *MNRAS*, 503, 2014

Teissier J.-M., Mäusle R., Müller W.-C., 2024, *J. Comput. Phys.*, 515, 113287

Tissot G., Mémín É., Jamet Q., 2024, in: Chapron B., Crisan D., Holm D., Mémin E., Radomska A. (eds), *Stochastic Compressible Navier–Stokes Equations*. Under Springer Nature Switzerland, p. 293, preprint (arXiv:2309.12077)

Turkel E., 1999, *Ann. Rev. Fluid Mech.*, 31, 385

Verma M. K., Donzis D., 2007, *J. Phys. A: Math. Theor.*, 40, 4401

Waagan K., Federrath C., Klingenberg C., 2011, *J. Comput. Phys.*, 230, 3331

Wagstaff J. M., Banerjee R., Schleicher D., Sigl G., 2014, *Phys. Rev. D*, 89, 103001

Yee K., 1966, *IEEE Trans. Antennas Propag.*, 14, 302

APPENDIX A: CHOICE OF THE CUT-OFF MACH NUMBER (M_{cut})

Fluxes obtained from an approximate Riemann solvers have a dissipation term in the momentum/pressure flux of the form

$$D \sim \rho \lambda_{\text{fastest}} (u^L - u^R), \quad (\text{A1})$$

where ρ and λ_{fastest} are suitable approximations of density and the fastest wave speed at the cell interfaces, and u^L and u^R are the x-components (direction along which the MHD equations are one-dimensionalized before solving the Riemann problem) of the fluid speed on the left and right side of the cell interface, respectively. This dissipation term adds artificial viscosity that dampens down any spurious perturbation modes generated in the solution of the discretized MHD equations. However, in the low-Mach regime, such a dissipation term overwhelms the physical flux. This is clear from the ratio of the advective flux to the dissipation term:

$$\frac{F_{\text{advective}}}{D} \sim \frac{\rho u^2}{\rho \lambda_{\text{fastest}} \Delta u} \sim \mathcal{M}. \quad (\text{A2})$$

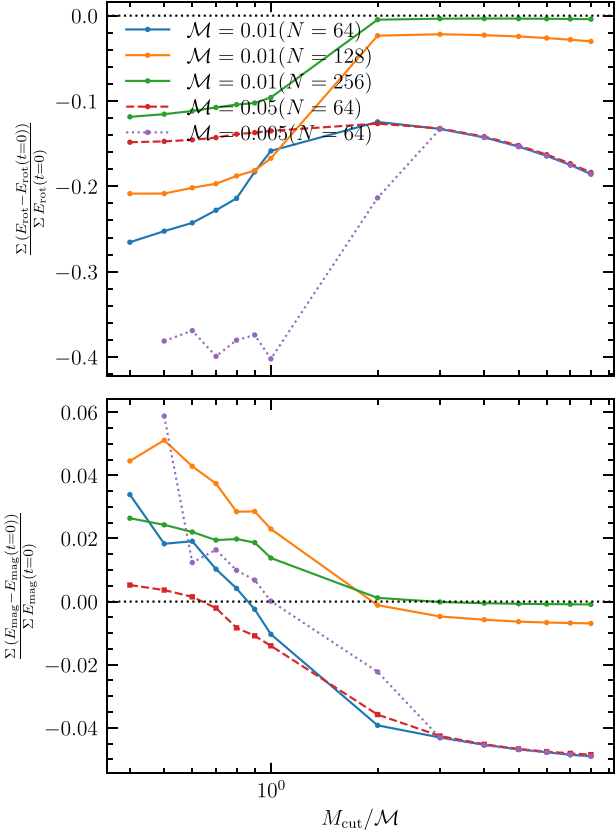


Figure A1. Variation of the amount of rotational (top panel) and magnetic energy (bottom panel) dissipated at the end of one advection as a function of $M_{\text{cut}}/\mathcal{M}$ at various Mach numbers ($M=0.005, 0.01, 0.05$) and resolutions ($M=0.01$ at $N=64, 128, 256$). For $M_{\text{cut}}/\mathcal{M} \leq 1$, there is a spurious increase in the magnetic energy and the dissipation of rotational energy. $M_{\text{cut}}/\mathcal{M} \gtrsim 1$ provides a fairly universal choice that provides stable, physical solutions with low dissipation. We chose $M_{\text{cut}}/\mathcal{M} = 2$ for our 64×64 test at Mach 0.01.

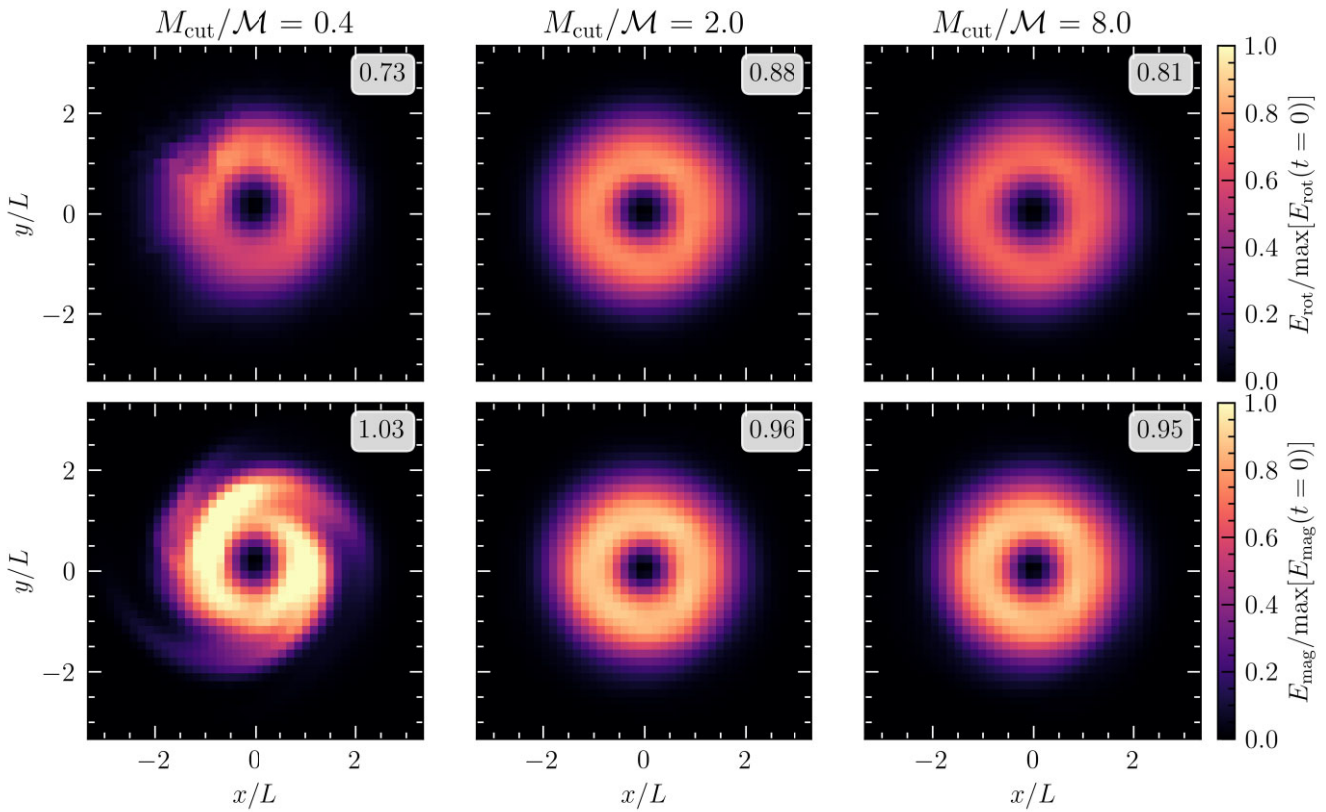


Figure A2. Rotational (top panel) and magnetic energy (bottom panel) profile of the vortex at the end of one advection for $M_{\text{cut}}/\mathcal{M} = 0.4, 2$ and 8 . $M_{\text{cut}}/\mathcal{M} \leq 1$ shows a spurious increase in the magnetic energy and distorts the vortex. In contrast, $M_{\text{cut}}/\mathcal{M} \gtrsim 1$ yields stable, low-dissipation solutions.

The advective flux is smaller compared to the dissipation term in subsonic flows.

This incorrect scaling is fixed by rescaling the dissipation term by a factor $\phi \propto \mathcal{M}$. C. Birke & C. Klingenberg (2023) use $\phi = M_{\text{BK}}$ defined in equation (14) as

$$M_{\text{BK}} = \min \left\{ \max \left\{ M_{\text{cut}}, \frac{u}{c_s} \right\}, 1 \right\}. \quad (\text{A3})$$

M_{cut} sets a local cut-off Mach number below which dissipation is no longer reduced. It also controls the fastest wave-speed in the relaxation scheme (see equation (13)). Our relaxation scheme is less diffusive as long as $M_{\text{cut}} < 1$.

Here, we explore the effect of M_{cut} . We run simulations of the Balsara Vortex test problem at $\mathcal{M} = 0.01$ at resolutions of 64^2 , 128^2 and 256^2 for $M_{\text{cut}}/\mathcal{M}$ ranging from 0.4 to 8. We also run additional tests, at $\mathcal{M} = 0.005$ and $\mathcal{M} = 0.05$ at 64^2 resolution. Fig. A1 shows the amount of rotational (top panel) and magnetic energy (bottom panel) dissipated at the end of one complete advection of the vortex. For $M_{\text{cut}}/\mathcal{M} \leq 1$, there is an increase in the rotational energy dissipation and a spurious increase in the magnetic energy is also seen. This spurious increase in the magnetic energy corresponds to a significant distortion of the vortex. An example of such a distortion is shown in the left most panel of Fig. A2, which shows the profile of the rotational (top panel) and the magnetic energy (bottom panel)

corresponding to $M_{\text{cut}}/\mathcal{M} = 0.4, 2$ and 8 for the 64×64 run at Mach 0.01.

In Fig. A1, $M_{\text{cut}}/\mathcal{M} = 2$ shows the least dissipation of rotational kinetic energy and conserves the magnetic energy well. Therefore, we choose this value for our vortex test. We also perform a resolution test measuring the L_1 norm of the rotational kinetic energy and the magnetic energy for USM-BK (at $M_{\text{cut}}/\mathcal{M} = 2$) and USM-HLLD. The L_1 for energy E (rotational or magnetic) is calculated using

$$L_1(E) = \frac{\sum |E - E(t=0)|}{\sum E(t=0)}. \quad (\text{A4})$$

The variation of the L_1 norm with the number of resolution elements in the x/y direction (N) are shown in Fig. A3. USM-HLLD has a higher value of L_1 norm compared to USM-BK and it decreases with increasing resolution for both of them. This shows that USM-BK performs better than USM-HLLD and there is no growth of dispersive errors.

It is clear that the optimal choice of $M_{\text{cut}}/\mathcal{M}$ is Mach number-dependent and may depend on the type of problem too. For a given MHD problem, the optimal value can be inferred from low-resolution runs before the solver is used in the corresponding high-resolution production run. Nevertheless, the parameter variation tests in Fig. A1 suggest that $M_{\text{cut}}/\mathcal{M} \gtrsim 1$ provides a relatively universal choice that yields stable and low-dissipation solutions with USM-BK.

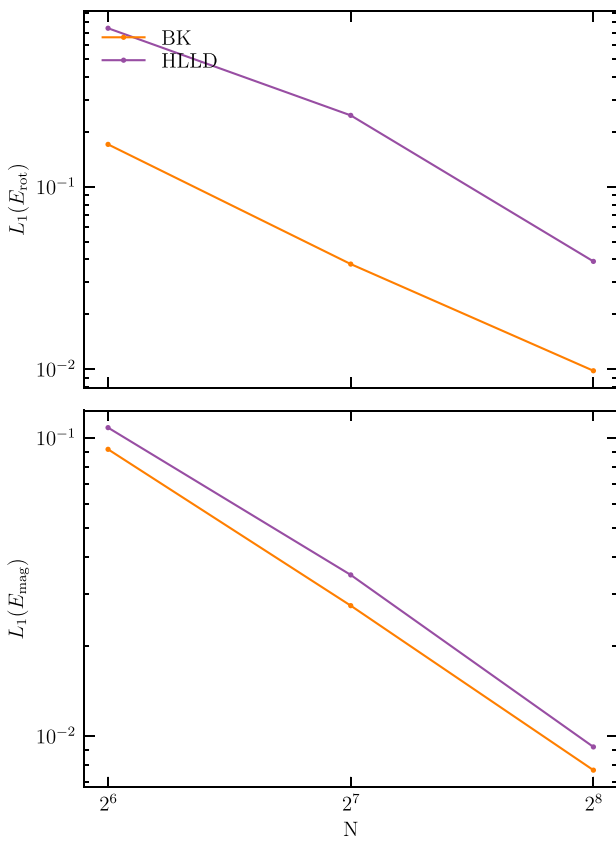


Figure A3. Variation of the L_1 norm with increasing resolution. N is the number of resolution elements in the x/y direction and L_E is calculated via equation (A4). USM-BK performs better than USM-HLLD and the error decreases with increasing resolution for both of them, implying that neither show any growth of dispersive errors, with $M_{\text{cut}}/\mathcal{M} = 2$ is a good choice for USM-BK.

APPENDIX B: EFFECTIVE HYDRODYNAMIC AND MAGNETIC REYNOLDS NUMBERS

The hydrodynamic Reynolds number (Re) is defined as

$$\text{Re} = \frac{u_{\text{turb}} \ell_{\text{turb}}}{\nu}, \quad (\text{B1})$$

where u_{turb} is the fluid turbulent velocity at the driving scale of turbulence ($\ell_{\text{turb}} = 2\pi/k_{\text{driving}}$) and ν is the kinematic viscosity of the fluid. Similarly, the magnetic Reynolds number (Rm) is defined as

$$\text{Rm} = \frac{u_{\text{turb}} \ell_{\text{turb}}}{\eta}, \quad (\text{B2})$$

where η is the magnetic resistivity of the fluid.

Numerical viscosity and resistivity must be lower than the explicit viscosity and resistivity to avoid smearing of features and over-

damping of flows. Therefore, the numerical Reynolds numbers associated with a numerical scheme must be greater than the explicit Reynolds number being simulated. We can calculate the numerical Hydrodynamic Reynolds number and Magnetic Prandtl number of ideal MHD simulations from measurements of the characteristic dissipation scales.

To calculate the hydrodynamic Reynolds number, we use the following relation given in N. Kriel et al. (2022)

$$\text{Re} = \left(\frac{k_v}{c_v k_{\text{driving}}} \right)^{4/3}, \quad (\text{B3})$$

where $c_v = 0.025^{+0.005}_{-0.006}$ (referred to as c_{Re} in the main text).

To measure the magnetic Reynolds number, we follow N. Kriel et al. (2025). However, their definition of the resistive dissipation scale (their definition will be referred to as k'_v) is different from what we have used in equation (24). They define the viscous dissipation wave-number as the wave-number where the scale-dependent hydrodynamic Reynolds number equals one, i.e. $\text{Re}(k'_v) = 1$. This wave-number marks the scale where the flow transitions from an inertial force dominated one ($k_{\text{turb}} < k < k'_v$) to a dissipation-dominated one ($k > k'_v$). N. Kriel et al. (2025) have shown that k'_v and Re are related by

$$k'_v = c'_v k_{\text{driving}} \text{Re}^{3/4}, \quad (\text{B4})$$

where $c'_v = 0.10^{+0.01}_{-0.01}$.

Using equation (B3) and equation (B4), we can write

$$k'_v = \frac{c'_v}{c_v} k_v. \quad (\text{B5})$$

Thus, if we have measured k_v from spectral fitting in equation (24), we can find k'_v .

N. Kriel et al. (2025) have also shown the resistive dissipation wave-number (k_η) scales with the viscous dissipation wave-number (k'_v , based on the alternative definition mentioned here) and the Prandtl number as

$$k_\eta = c_\eta k'_v \text{Pm}^{1/2}, \quad (\text{B6})$$

where $c_\eta = 0.53^{+0.07}_{-0.07}$.

Using equation (B5) and equation (B6), we can write

$$k_\eta = c_\eta \frac{c'_v}{c_v} k_v \text{Pm}^{1/2} = c_{\text{Pm}} k_v \text{Pm}^{1/2}, \quad (\text{B7})$$

where $c_{\text{Pm}} = c_\eta c'_v / c_v = 2.1^{+0.8}_{-0.5}$.

The Prandtl number (Pm) can be obtained using the above relation. The Magnetic Reynolds number can then be calculated as

$$\text{Rm} = \text{Re} \times \text{Pm}. \quad (\text{B8})$$

This paper has been typeset from a TeX/LATEX file prepared by the author.